14

Crystalization in Spinel Ferrite Nanoparticles

Mahmoud Goodarz Naseri[1,2] and Elias B. Saion[1]
[1]*Universiti Putra Malaysia,*
[2]*Malayer University,*
[1]*Malaysia*
[2]*Iran*

1. Introduction

The enhanced interest of the researchers in nanoobjects is due to the discovery of unusual physical and chemical properties of these objects, which is related to manifestation of so-called 'quantum size effects'. These arise in the case where the size of the system is commensurable with the de-Brogli wavelengths of the electrons, phonons or excitons propagating in them.A key reason for the change in the physical and chemical properties of small particles as their size decreases is the increased fraction of the surface atoms, which occur under conditions (coordination number, symmetry of the local environment, etc.) differing from those of the bulk atoms. From the energy standpoint, a decrease in the particle size results in an increase in the fraction of the surface energy in its chemical potential [1]. Currently, unique physical properties of nanoparticles are under intensive research [2]. A special place belongs to the magnetic properties in which the difference between a massive (bulk) material and a nanomaterial is especially pronounced.The magnetic properties of nanoparticles are determined by many factors, the key of these including the chemical composition, the type and the degree of defectiveness of the crystal lattice, the particle size and shape, the morphology (for structurally inhomogeneous particles), the interaction of the particle with the surrounding matrix and the neighbouring particles. By changing the nanoparticle size, shape, composition and structure, one can control to an extent the magnetic characteristics of the material based on them. However, these factors cannot always be controlled during the synthesis of nanoparticles nearly equal in size and chemical composition; therefore, the properties of nanomaterials of the same type can be markedly different [1].Apart from these factors, the magnetic properties of particles depend on the external conditions: temperature, pressure and, in some cases, the local environment, i.e., the medium in which the particle occurs, in particular, the crystalline or amorphous bulk matrix (for a particle), the local crystal environment (for a single atom) or the substrate (for a film).

2. Ferrites and their structural symmetries

Among the magnetic materials that have found broad practical application in technology, ferrites deserve attention. Ferrite nanoparticles are the most explored magnetic nanoparticles up to date. They are widely used in high-frequency applications, because an AC field does not induce undesirable eddy currents in an insulating material [3,4].To increase the recorded information density, it seems reasonable to obtain nanocrystalline

ferrites and to prepare magnetic carriers based on them. Ferrites have three different structural symmetries: garnet, hexagonal and cubic which are determined by the size and charge of the metal ions that balance the charge of the oxygen ions, and their relative amounts [5]. In this review, the focus will be on spinel ferrites nanocrystals because, they are regarded as two of the most important inorganic nanomaterials because of their electronic, optical, electrical, magnetic, and catalytic properties.Moreover, the majority of the important ferrite are spinel ferrite [6].

2.1 Garnets ferrites

The general formula for garnets is $Me_3Fe_5O_{12}$, where Me is one of the rare earth metal ions, including Y, La and Gd. The cubic unit cell contains 8 formula units or 160 atoms, which can be described as a spatial arrangement of 96 O^{2-} with interstitial cations. Yttrium iron garnet $Y_3Fe_5O_{12}$ (YIG) is a well-known garnet. The coordination of the cations is considerably more complex than spinels, with 24 Y^{3+} in dodecahedral sites, 24 Fe^{3+} ions in tetrahedral sites and 16 remaining Fe^{3+} in octahedral sites. Similar to spinels and hexagonal ferrites, a wide range of transition metal cations can substitute Y^{3+} or Fe^{3+}; especially rare earth ions may replace the ions on octahedral and dodecahedral sites. Each type of lattice site will accept other metal ions at dodecahedral sites, octahedral sites and at tetrahedral sites. Thus pentavalent ions such as V^{5+} and As^{5+} can occupy tetrahedral sites, while Ca2+ substitute ions on dodecahedral sites [7].

2.2 Hexagonal ferrites

Hexagonal ferrites are widely used as permanent magnets and are characterized by possesing a high coercivity [4].Their general formula is $MeO \cdot 6Fe_2O_3$ where Me can be Ba, Sr, or Pb. The hexagonal ferrite lattice is similar to the spinel structure, with the oxygen ions closely packed, but some layers include metal ions, which have practically the same ionic radii as the oxygen ions. This lattice has three different sites occupied by metals: tetrahedral, octahedral, and trigonal bi pyramid (surrounded by five oxygen ions).

2.3 Cubic ferrites

Materials which crystallize in the spinel structure, or structures closely related to it, have the general formula AB_2O_4 in which A and B display tetrahedral and octahedral cation sites, respectively, and O indicates the oxygen anion site (Figure1). Spinel ferrites with the general formula $MeO\ Fe_2O_3$ or $Me^{II}Fe_2^{III}O_4$ where Me^{II} represents a divalent metal cation such as Mn, Fe, Co, Ni, Cu, Zn, Cd, Mg, or $(0.5Li^{I} + 0.5Fe^{III})$, and Fe^{III} is the trivalent iron cation, have the same crystallographic structure as the mineral spinel ($MgAl_2O_4$), which was determined by Bragg [8,9]. The unit cell of spinel ferrite belongs to the cubic structure (space group Oh7-F3dm) and presents itself the cube formed by 8 $MeOFe_2O_3$ molecules and consisting of 32 of O^{2-} anions. The oxygene anions form the close face-centered cube (FCC) packing consisting in 64 tetrahedral (A) and 32 octahedral (B) empty spaces partly populated by Fe^{3+} and Me^{2+} cations [10].

For the interactions the distances Me-O and Me-O-Me play an important role, ten triangular configurations of Me-O-Me are illustrated in Figure2, where the shortest distance is shown as p and other distances are given by q, r, s and t; these distances are also given in Table1, as a function of the variable $\delta = u - 3/8$ that δ is oxygen parameter [11].

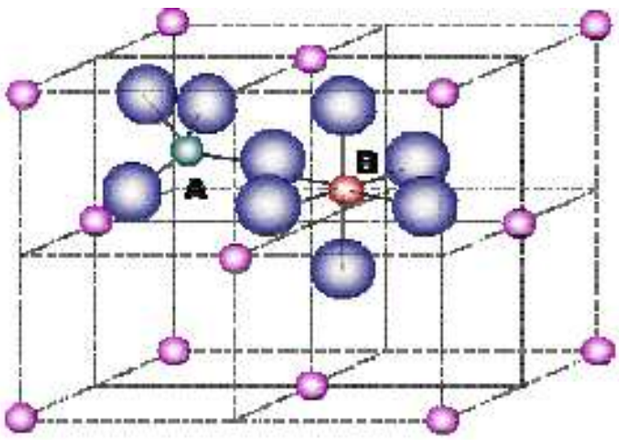

Fig. 1. Schematic of two subcells of a unit cell of the spinel structure, showing octahedral and tetrahedral sites.

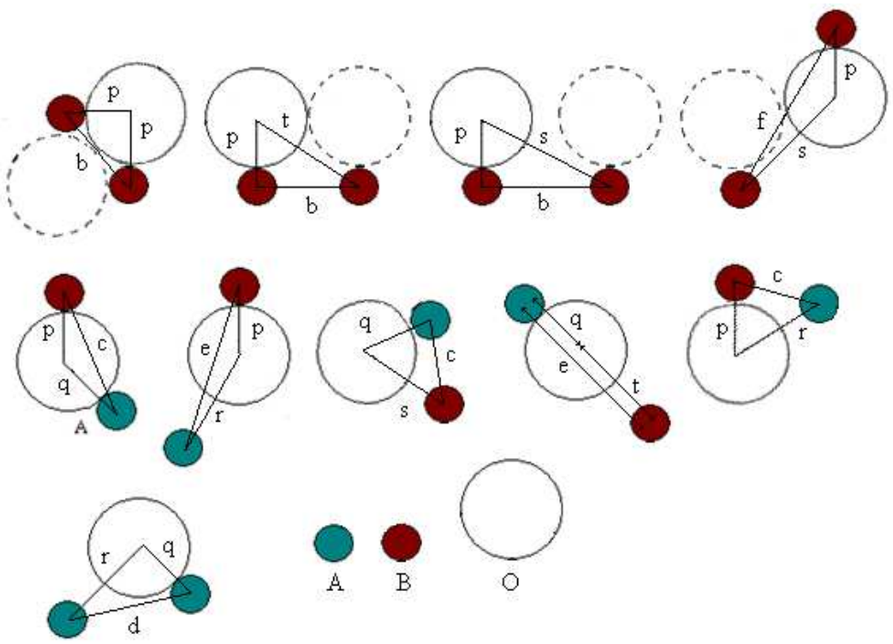

Fig. 2. Interionic distances in the spinel structure for the different types of lattice site interactions

According to the distribution of cations, there are normal, mixed and inversed spinels structures which depended on the fact what kind of ions and in what order A and B take empty spaces. In this review, we will investigate zinc ferrite ($ZnFe_2O_4$), manganese ferrites ($MnFe_2O_4$) and nickel ferrite ($NiFe_2O_4$) from normal, mixed and inverse structures respectively [12].

Me-O distance	Me-Me distance
$\mathbf{p = a\sqrt{\frac{1}{16} - \frac{1}{2}\delta + 3\delta^2}}$	$b = \frac{1}{4}a\sqrt{2}$
$\mathbf{q = \left(\frac{1}{8} + \delta\right)\sqrt{3}}$	$c = \frac{1}{8}a\sqrt{11}$
$\mathbf{r = a\sqrt{\frac{1}{24} + \frac{1}{4}\delta + 3\delta^2}}$	$d = \frac{1}{4}a\sqrt{3}$
$\mathbf{s = a\sqrt{\frac{3}{16} + \frac{1}{2}\delta + 3\delta^2}}$	$e = \frac{3}{8}a\sqrt{3}$
$\mathbf{t = a\left(\frac{1}{4} - \delta\right)\sqrt{3}}$	$f = \frac{1}{4}a\sqrt{6}$

Table 1. Distances in the spinel lattice as a function of δ=u-3/8

2.3.1 Normal spinel ferrites

Normal spinel structure, where all Me^{2+} ions occupy A sites; structural formula of such ferrites is $Me^{2+}[Fe_2{}^{3+}]\ O_4{}^{2-}$. This type of distribution takes place in zinc ferrites $Zn^{2+}[Fe^{2+}Fe^{3+}]O_4{}^{2-}$. This type spinel ferrite are schematically illustrated in Figure3.

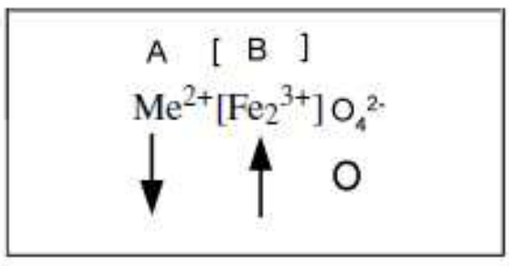

Fig. 3. Cation distribution in normal spinel ferrites.

2.3.2 Mixed spinel ferrites

Mixed spinel structure, when cations Me^{2+} and Fe^{3+} occupy both A and B-positions; structural formula of this ferrite is $Me_{1-\delta}{}^{2+}Fe_{\delta}{}^{3+}\ [Me_{\delta}{}^{2+}Fe_{2-\delta}{}^{3+}]\ O_4{}^{2-}$, where δ is the degree of inversion. $MnFe_2O_4$ represent this type of structure and has an inversion degree of δ = 0.2 and its structural formula therefore is $Mn_{0.8}{}^{2+}Fe_{0.2}{}^{3+}\ [Mn_{0.2}{}^{2+}Fe_{1.8}{}^{3+}]\ O_4{}^{2-}$. [12]. This type spinel ferrite are schematically illustrated in Figure4.

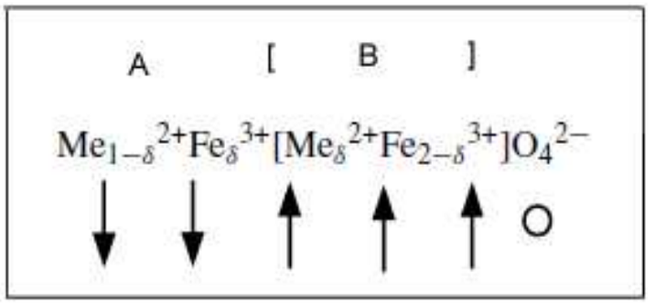

Fig. 4. Cation distribution in mixed spinel ferrites.

2.3.3 Inversred spinel ferrites

Inversed spinel structure, where all Me^{2+} are in B-positions and Fe^{3+} ions are equally distributed betweenAand B-sites: structural formula of these ferrites are $Fe^{3+}[Me^{2+}Fe^{3+}]\ O_4^{\ 2-}$. Magnetite Fe_3O_4, ferrites $NiFe_2O_4$ and $CoFe_2O_4$ have inversed spinel structure [12].In the inversed ferrites one half of Fe^{3+} is placed in A-sites and another half in B-sites. Their magnetic moments are mutually compensated and the resulting moment of the ferrite is due to the magnetic moments of bivalent cations Me^{2+} in the B-positions. This type spinel ferrite are schematically illustrated in Figure5.

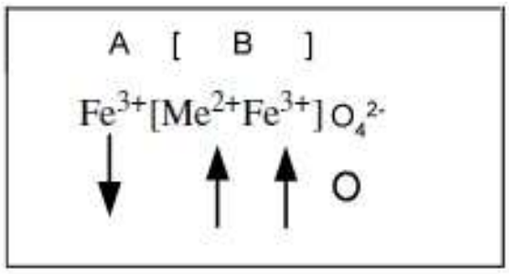

Fig. 5. Cation distribution in inversed spinel ferrites.

2.4 Domains

Domains, which are groups of spins all pointing in the same direction and acting cooperatively are separated by domain walls, which have a characteristic width and energy associated with their formation and existence. The motion of domain walls is a primary means of reversing magnetization. Experimental investigation of the dependence of coercivity on particle size showed a behavior similar to that schematically illustrated in Figure 6 [13].

It was found that the coercivity H_c increases with decreasing grain size D down to values of about 40 nm, independent of the kind of material. The increase of H_c is proportional to 1/D. The reason for this is that in small particles the formation of a closed magnetic flux becomes energetically less favorable so that the magnetic domain size with a uniform magnetization becomes more and more identical with the grain size. This grain size is defined as the first critical size (D_c, which is characteristic of each material) where the multidomain materials

change to a monodomain material. This leads to a strong increase of the coercivity (or high remanence) because a change of magnetization in this case cannot happen only by shifting the domain walls which normally requires only a weak magnetic field. As the size of magnetic element scales below20 nm, the transformation from ferromagnetic to superparamagnetic behavior occurs. In the superparamagnetic state of the material, the room temperature thermal energy overcomes the magnetostatic energy well of the domain or the particle, resulting in zero hysteresis. In other words, although the particle itself is a single-domain ferromagnet, the ability of an individual magnetic "dot" to store magnetization orientation information is lost when its dimension is below a threshold. Consequently, the magnetic moments within a particle rotate rapidly in unison, exhibiting the superparamagnetic relation phenomenon.

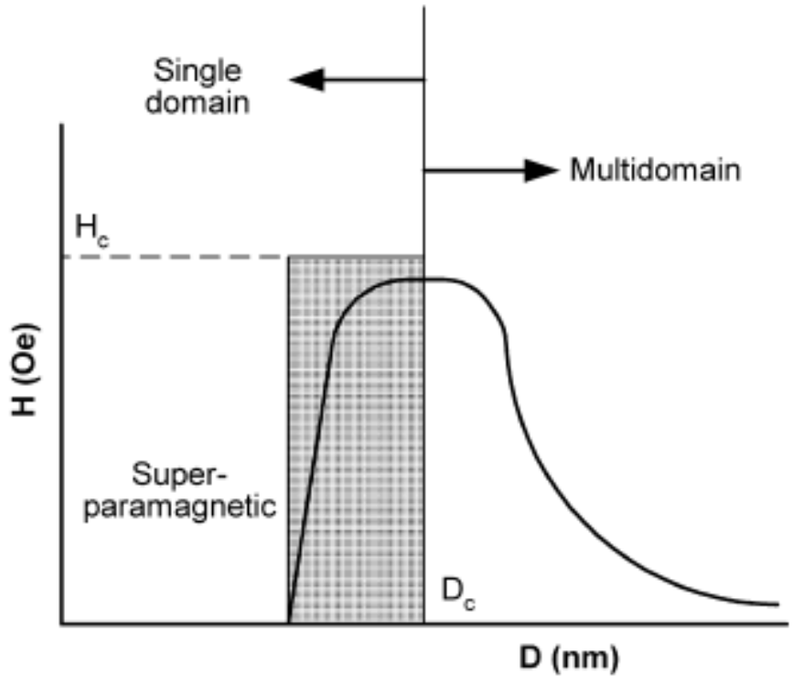

Fig. 6. Qualitative illustration of the behavior of the coercivity in ultrafine systems as the particle size changes, where H is the magnetic field amplitude (Oe) and *D* is the particle diameter (nm).

a. *Magnetostatic or demagnetization energy:* The magnetized material behaves like a magnet, with a surrounding magnetic field. This field acts to magnetize the material in the direction opposite from its own magnetization, causing a magnetostatic energy which depends on the shape of the material. This magnetostatic energy can be reduced by reducing the net external field through the formation of domains inside the material.
b. *Magnetocrystalline anisotropy energy:* In some materials the domain magnetization tends to align in a particular crystal direction (the so-called easy axis). The material is easiest to magnetize to saturation or demagnetize from saturation if the field is applied along an easy axis. The energy difference between aligning the domain in the easy and another direction (hard direction) is called magnetocrystalline anisotropy energy. Anisotropy energy is the energy needed to rotate the moment from the easy direction to

a hard direction. For materials with cubic crystalline structure (such as ferrites), the energy is expressed in terms of anisotropy constants and the direction to which the magnetization rotates.

$$E_k=K_1\sin^2\theta+K_2\sin^4\theta\ldots \text{ (Hexagonal structre)}$$

$$E_k=K_1(\alpha_1^2\alpha_2^2+\alpha_2^2\alpha_3^2+\alpha_3^2\alpha_1^2)+K_2(\alpha_1^2\alpha_2^2\alpha_3^2+\ldots)\text{ (Cubic and Garnet structure)} \quad (1)$$

where K is the anisotropy constant, θ is the angle between the easy axis and the direction of magnetization, and a ; are the direction cosines, which are the ratios of the individual components of the magnetization projected on each axis divided by the magnitude of the magnetization. A crystal is higher in anisotropy energy when the magnetization points in the hard direction rather than along the easy direction. The formation of domains permits the magnetization to point along the easy axis, resulting in a decrease in the net anisotropy energy.

c. *Magnetostrictive energy:* In a magnetic field, the material may change its dimensions on the order of several parts per million. This change in dimension results in what is called magnetostrictive energy, which is lowered by a reduction in the size of the domains, requiring the formation of more domains.

2.5 Magnetization curve and hysteresis loops

The magnetization curve describes the change in magnetization or magnetic flux of the material with the applied field. When a field is applied to a material with randomly oriented magnetic moments, it will be progressively magnetized due to movement of domain boundaries. Initially, when no field is applied, the magnetic dipoles are randomly oriented in domains, thus the net magnetization is zero. When a field is applied, the domains begin to rotate, increasing their size in the case of the domains with direction favorable with respect to the field, and decreasing for the domains with unfavorable direction. As the field increases, the domains continue to grow until the material becomes a single domain, which is oriented in the field direction. At this point, the material has reached saturation (Figure7) [3].As the magnetic field is increased or decreased continuously, the magnetization of the material increases or decreases but in a discontinuous fashion. This phenomenon is called the Barkhausen effect and is attributed to discontinuous domain boundary motion and the discontinuous rotation of the magnetization direction within a domain [14]. The typical magnetization curve can be divided into three regions:

a. *Reversible region:* The material can be reversibly magnetized or demagnetized. Charges in magnetization occur due to rotation of the domains with the field.
b. *Irreversible region:* Domain wall motion is irreversible and the slope increases greatly.
c. *Saturation region:* Irreversible domain rotation. It is characterized by a required large amount of energy to rotate the domains in the direction of the field [5].

If the field is reduced from saturation, with eventual reversal of field direction, the magnetization curve does not retrace its original path, resulting in what is called a hysteresis loop. This effect is due to a decrease of the magnetization at a lower rate. The area inside the hysteresis loop is indicative of the magnetic energy losses during the magnetization process. When the field reaches zero, the material may remain magnetized (i.e., some domains are

oriented in the former direction). This residual magnetization is commonly called remanence M_r. To reduces this remanent magnetization to zero; a field with opposite direction must be applied. The magnitute of field required to lower the sample magnetization to zero is called the coercivity H_c (Figure 8). A material can present different hysteresis loops depending on the degree of magnetization. If the maximum magnetization is less than the saturation magnetization, the loop is called a minor loop [3,4].

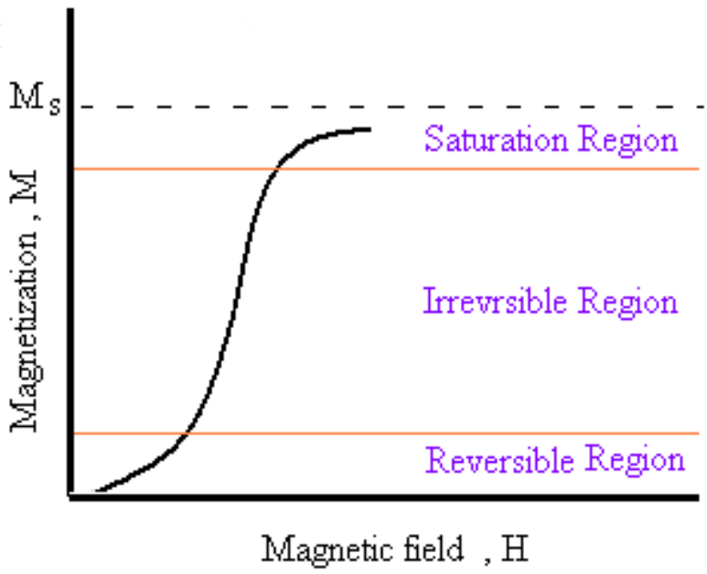

Fig. 7. Magnetization curve with domain configurations at different stages of magnetization.

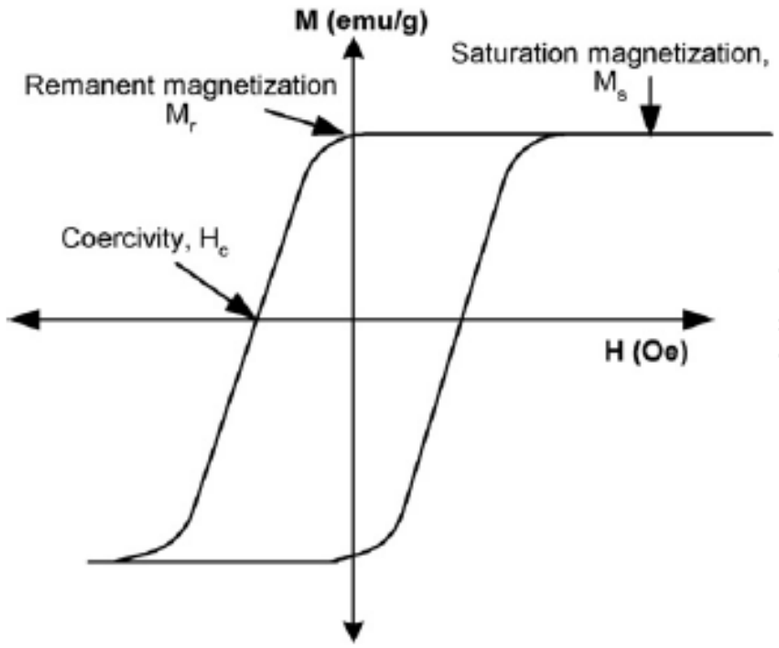

Fig. 8. Hysteresis cycle of a multidomain magnetic material, where*H*is the magnetic field amplitude (Oe) and M is the magnetization of the material (emu/g).

2.6 Magnetic behaviors

Ferrites materials can be classified based on differences between their internal and external flux and the variation of the magnetization M or magnetic induction B when a magnetic field is applied (Figure 9) [3,4]. There are two quantities that relate M and B to H: the susceptibility χ and the permeability μ .

$$\chi = \frac{M}{H}, \tag{2}$$

$$\mu = \frac{B}{H}. \tag{3}$$

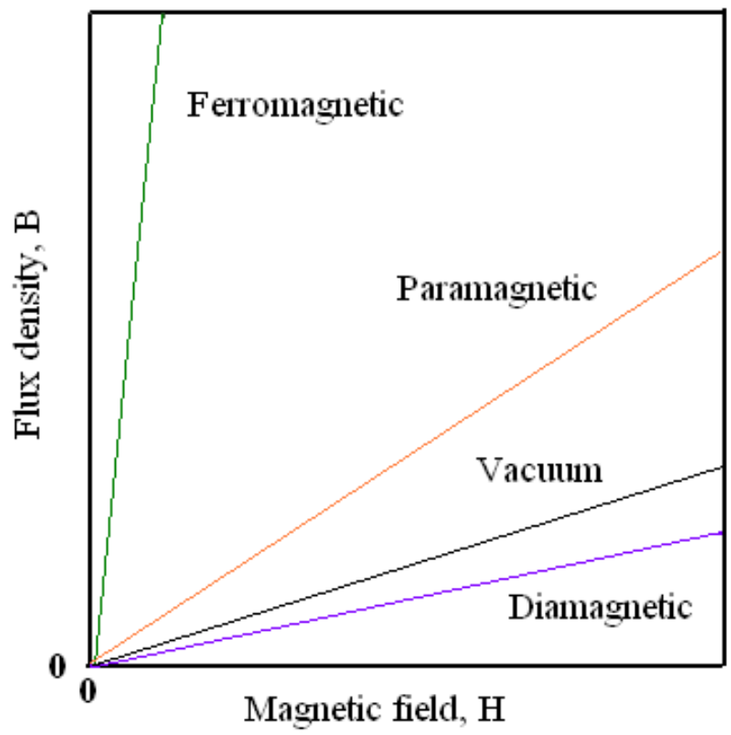

Fig. 9. Representation of the behavior of the flux density with respect to the magnetic field for different classes of magnetic materials.

In SI the permeability μ has units of Henry/m. The susceptibility is a measure of the increase in magnetic moment caused by an applied field, whereas permeability represents the relative increase in flux caused by the presence of the magnetic material [15].

2.6.1 Diamagnetism

Diamagnetism is an inherent result of the orbital motion of the electrons in a magnetic field. It is present when the atom has zero net magnetic moment. In this case the orbital motion generates a field opposite to the applied field (magnetization is directed oppositely to the

field, as illustrated in Figure 10), described by a negative susceptibility. These materials tend to move toward regions of weaker field [5, 15].

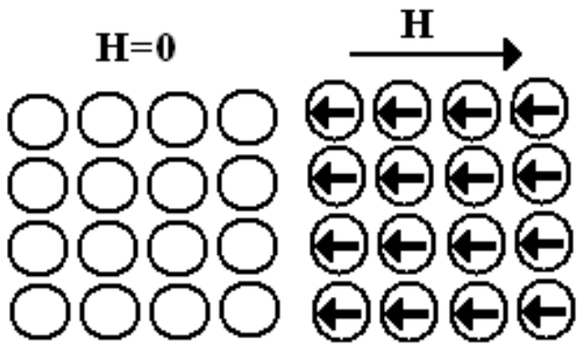

Fig. 10. Atomic dipole configuration for a diamagnetic material.

2.6.2 Paramagnetism

Paramagnetic materials possess a permanent dipole moment due to incomplete cancellation of electron spin and/or orbital magnetic moments. In the absence of an applied magnetic field the dipole moments are randomly oriented; therefore the material has no net macroscopic magnetization. When a field is applied these moments tend to align by rotation towards the direction of the field and the material acquires a net magnetization (Figure 11) [3].

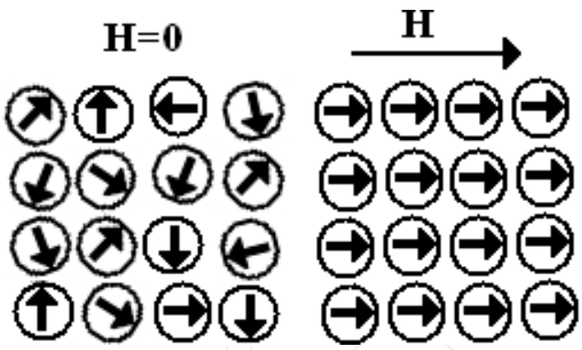

Fig. 11. Schematic of atomic dipoles for a paramagnetic material.

2.6.3 Ferromagnetism and ferrimagnetism

Ferro and ferri-magnetic materials possess a permanent magnetic moment in the absence of an external field and a very large permanent magnetization [3]. In ferromagnetic materials, this permanent magnetic moment is the result of the cooperative interaction of large numbers of atomic spins in what are called domains, regions where all spins are aligned in the same direction (see section2.5).In ferrimagnetic materials, on the other hand, incomplete cancellation of the magnetic dipoles in a domain results in lower permanent magnetization (Figure 12) [5].

The macroscopic magnetization of ferro- and ferri-materials is the sum of the magnetizations of the domains which make up the sample [3]. Ferrimagnets are ionic solids meaning that they are electrically insulating, whereas most ferromagnets are metals (conductors) [4].

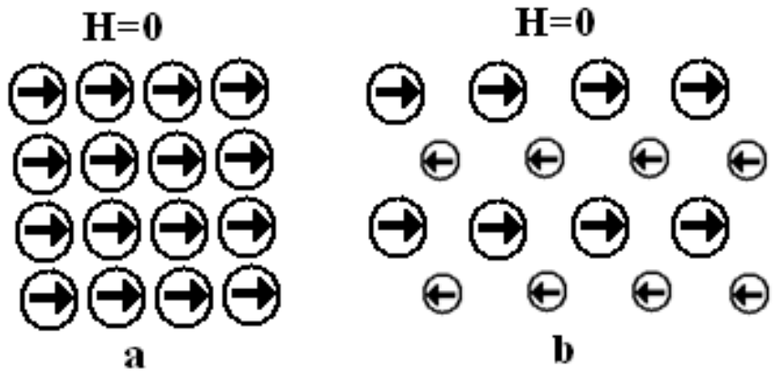

Fig. 12. Ordering of the atomic dipoles in a) ferromagnetic and b) ferrimagnetic material.

2.6.4 Antiferromagnetism

In materials that exhibit antiferromagnetism, the magnetic moments of atoms or molecules, usually related to the spins of electrons, align in a regular pattern with neighboring spins (on different sublattices) pointing in opposite directions. This is, like ferromagnetism and ferrimagnetism, a manifestation of ordered magnetism. Generally, antiferromagnetic order may exist at sufficiently low temperatures, vanishing at and above a certain temperature, the Néel temperature (Neel temperature is the temperature at which an antiferromagnetic material becomes paramagnetic; hence losing its magnetic properties) [16].Above the Néel temperature, the material is typically paramagnetic. Figure13 shows ordering of the atomic dipoles in an antiferromagnetic material

Fig. 13. Ordering of the atomic dipoles in an antiferromagnetic material.

2.6.5 Superparamagnetic

Superparamagnetism is a phenomena by which magnetic materials may exhibit a behavior similar to paramagnetism at temperatures below the Neel or the Curie temperature (The Curie temperature is the temperature at which a ferromagnetic or a ferromagnetic material becomes paramagnetic; hence losing its magnetic properties).Normally, coupling forces in magnetic materials cause the magnetic moments of neighboring atoms to align, resulting in very large internal magnetic fields. At temperatures above the Curie temperature (or the Neel temperature for antiferromagnetic materials), the thermal energy is sufficient to overcome the coupling forces, causing the atomic magnetic moments to fluctuate randomly.

Because there is no longer any magnetic order, the internal magnetic field no longer exists and the material exhibits paramagnetic behavior. Superparamagnetism occurs when the material is composed of very small crystallites (lower than 100 nm). In this case even though the temperature is below the Curie or Neel temperature and the thermal energy is not sufficient to overcome the coupling forces between neighboring atoms, the thermal energy is sufficient to change the direction of magnetization of the entire crystallite. The resulting fluctuations in the direction of magnetization cause the magnetic field to average to zero. The material behaves in a manner similar to paramagnetism, except that instead of each individual atom being independently influenced by an external magnetic field, the magnetic moment of the entire crystallite tends to align with the magnetic field. The energy required to change the direction of magnetization of a crystallite is called the crystalline anisotropy energy (see section 2.5) and depends both on the material properties and the crystallite size. As the crystallite size decreases, so does the crystalline anisotropy energy, resulting in a decrease in the temperature at which the material becomes superparamagnetic [17]. Ordering of the atomic dipoles in a superparamagnetic material is shown in Figure 14.

Fig. 14. Ordering of the atomic dipoles in a superparamagnetic material.

2.7 Classification and applications of ferrites

Ferrites are grouped into two types, soft and hard. This is the classification based on their ability to be magnetized and demagnetized, not their ability to withstand penetration or abrasion. Soft materials are easy to magnetize and demagnetize, so are used for electromagnets, while hard materials are used for permanent magnets. They can also be classified based on their coercive field strength into soft and hard materials [12]. With soft magnetic materials the hysteresis loop is small (low coercive field strength, independent of magnetic field amplitude); with hard magnetic however it is large (high coercive field strength). Table 2 gives a comparative account of both types.

H_c < 10 A/Cm: soft magnetic;

H_c > 300 A/Cm: hard magnetic (permanent magnets).

Hard ferrite magnets are made in two different magnetic forms: isotropic and oriented. Isotropic magnets are formed to desired shapes, sintered and then magnetized. These exhibit a modest magnetic field and find applications in cycle dynamos and ring magnets. Oriented magnets are formed to shape under a strong magnetic field and then sintered. These exhibit a very strong magnetic field and find applications in loudspeakers, magnets of two wheelers like scooters, etc. [14].

Soft magnetic	Hard magnetic
High saturation magnetization (1-2T)	High saturation magnetization (0.3-1.6T)
Low coercivity (H_c)	High coercivity
High permeability	Not important, but low
Low anisotropy	High anisotropy
Low magnetostriction	Not important
High Curie temperature (T_c)	High T_c
Low losses	High-energy product
High electrical resistivity	Not important

Table 2. The comparative properties of soft and hard magnetic materials

3. Established methods for synthesis of nanocrystalline ferrites

There are two methods for the preparation of magnetic nanoparticles: physical and chemical. The methods of generation of magnetic nanoparticles in the gas or solid phase using high-energy treatment of the material are usually called physical, while the nanoparticle syntheses, which are often carried out in solutions at moderate temperatures are chemical methods. Different routes have become an essential focus of the related research and development activities. Various fabrication methods to prepare spinel ferrites nanocrystals have been reported, e.g., sol-gel methods [18], the ball-milling technique [19], co-precipitation [20], polymeric assisted route [21] the hydrothermal method [22], the reverse micelles process [23], and the micro-emulsion method [24]. Various precipitation agents have been used to produce specific size and shape spinel ferrites nanocrystals, e.g., metal hydroxide in the co-precipitation method, surfactant and ammonia in the reverse micelles process and various micro-emulsion methods, and organic matrices in the sol-gel method. Most of these methods have achieved particles of the required sizes and shapes, but they are difficult to employ on a large scale because of their expensive and complicated procedures, high reaction temperatures, long reaction times, toxic reagents and by-products, and their potential harm to the environment.

3.1 Thermal treatment method

In the present study, spinel ferrites nanocrystals with different structures were prepared from an aqueous solution containing metal nitrates, poly (vinyl pyrrolidon), and deionized water using a relatively low temperature thermal treatment method, followed by grinding and calcinations*. No other chemicals were added to the solution. This method is environmentally friendly in that it neither uses nor produces toxic substances, and it offers the advantages of simplicity, low cost, and low reaction temperatures. The textural and morphological characteristics of the spinel ferrites nanocrystals we prepared were studied with various techniques to determine the influence of calcination temperature on the crystallization, morphology, and particle size distribution of the nanocrystals and to explore other parameters of interest.

* This method was invented by Mahmoud Goodarz Naseri in university Putra Malaysia in 2011

3.1.1 Process of fabrication of metal ferrite nanocrystals

In this study, metal nitrate reagents, poly (vinyl pyrrolidon) (PVP), and deionized water were used as precursors. In addition, a capping agent to control the agglomeration of the particles and a solvent were used. Iron nitrate, $Fe(NO_3)_3 \bullet 9H_2O$, zinc nitrate, $Zn(NO_3)_2 \bullet 6H_2O$, nickel nitrate, $Ni(NO_3)_2 \bullet 6H_2O$, and manganese nitrate $Mn(NO_3)_2 \bullet 6H_2O$, were purchased from Acros Organics with a purity exceeding 99%. PVP (MW = 29000) was purchased from Sigma Aldrich and was used without further purification. An aqueous solution of PVP was prepared by dissolving polymer in deionized water at 363 K, before mixing 0.2 mmol iron nitrate and 0.1 mmol metal nitrate (Fe:M = 2:1) into the polymer solution and constantly stirring for 2 h using a magnetic stirrer until a colorless, transparent solution was obtained. The mixed solution was poured into a glass Petri dish and heated at 353 K in an oven for 24 h to evaporate the water. The dried, orange, solid zinc ferrite that remained was crushed and ground in a mortar to form powder. The calcinations of the powders were conducted at 723, 773, 823, and 873 K for 3 h for the decomposition of organic compounds and the crystallization of the nanocrystals. The processing steps employed separately for the synthesis of each ferrite nanoparticles.

3.2 Characterization

The textural and morphological characteristics of the spinel ferrite nanocrystals we prepared were studied with various techniques to determine the influence of calcination temperature on the crystallization, morphology, and particle size distribution of the nanocrystals and to explore other parameters of interest. The characterization of the prepared spinel ferrites nanoparticles were conducted by using various techniques such as to (TGA), X-ray diffraction (XRD), Fourier transforms infrared spectroscopy (FTIR), transmission electron microscopy (TEM), and vibrating sample magnetometer (VSM) verify the particle size and distribution and to explore other parameters of interest.in this section we introduce these techniques.

3.3 Mechanism of interaction of PVP and metal ions in synthesize of Zn, Mn and Ni ferrite nanoparticle by thermal treatment method

Interactions between the PVP capping agent [25] and metal ions are shown schematically in Figure 15.We have shown the Metal (II) (e.g. Zn, Mn and Ni) and iron (III) ions which are bound by the strong ionic bonds between the metallic ions and the amide group in a polymeric chain. PVP acts as a stabilizer for dissolved metallic salts through steric and electrostatic stabilization of the amide groups of the pyrolidine rings and the methylene groups. Initially, the PVP stabilizer may decompose to as limited extent, thereby producing shorter polymer chains that are capped when they are adsorbed onto the surfaces of metallic ions [26]. The metallic ions, which are well dispersed in the cavities and networks, are created as a result of the shorter polymer chains. These mechanisms continue until they are terminated by the drying step. The influence of PVP is not restricted only to the solution and the drying step; PVP also affects the formation of the nuclei (i.e., nucleation) of the nickel ferrite nanoparticles in the calcination step. In this step, the small nanoparticles with high surface energy levels would become larger via the Ostwald ripening process [27] without the presence of PVP, disrupts steric hindrance, thereby preventing their aggregation. Steric hindrance is a phenomenon that is attributed to large molecular weight (>10,000) and the repulsive forces acting among the polyvinyl groups [28, 29]. These interactions are similar to the stabilization of metallic nanoparticles, i.e., silver and gold [30, 31].

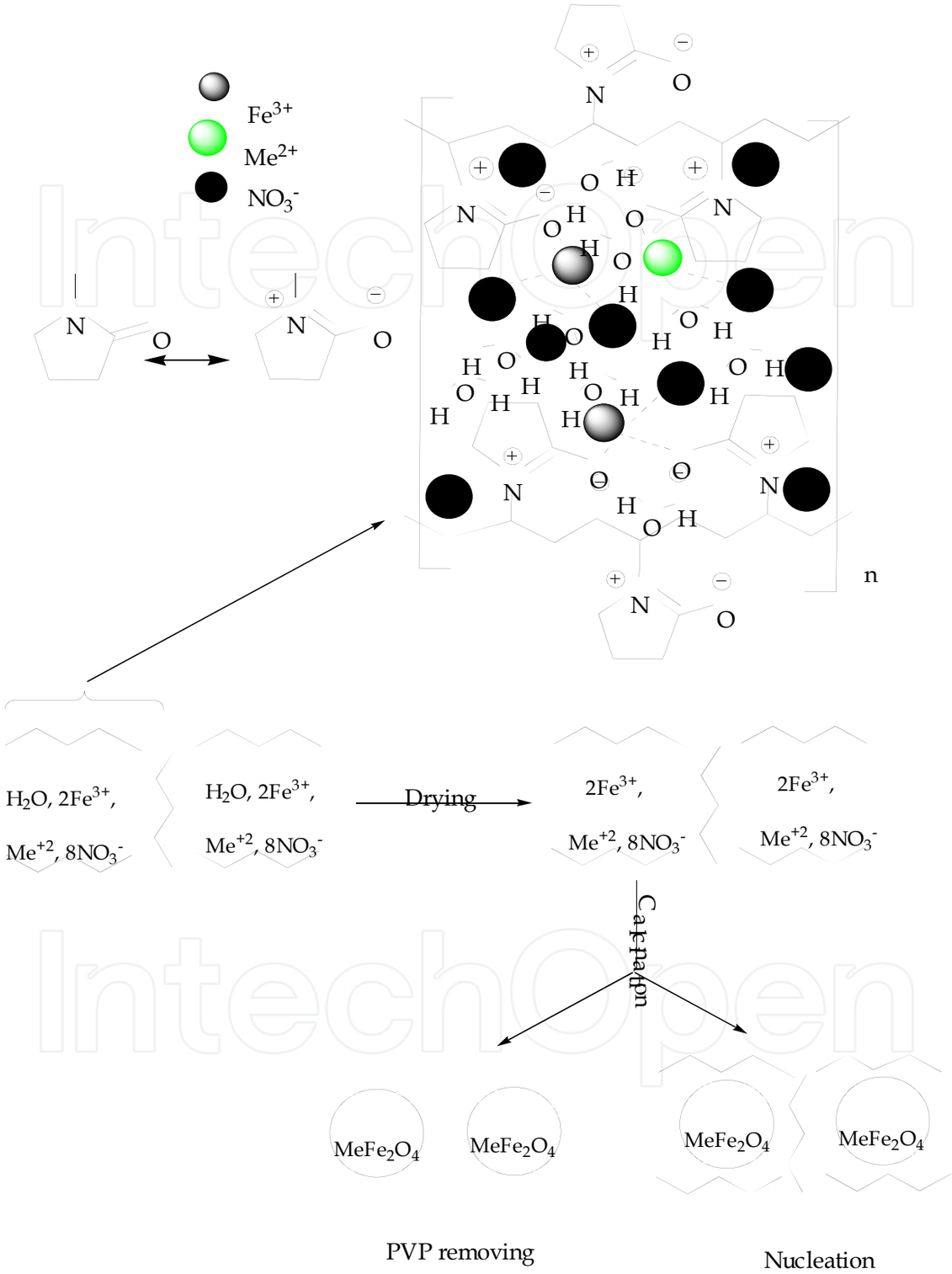

Fig. 15. The proposed mechanism of interactions between PVP and metal ions in the formation of the ferrites nanoparticles.

3.4 Determination of range of calcinations temperature for removing of PVP

Figure 16 shows the simultaneous thermal analyses (TG–DTG) for PVP. It is evident that this polymer exhibited only one mass loss which started at 678 K and its maximum rate decomposition temperature was located at 778 K. This confirms that the majority of the mass loss occurs under 778 K and allows for optimization of the heat treatment program. It is worth noting that several authors reported the thermal degradation of PVP exhibits only one mass loss [32-34].

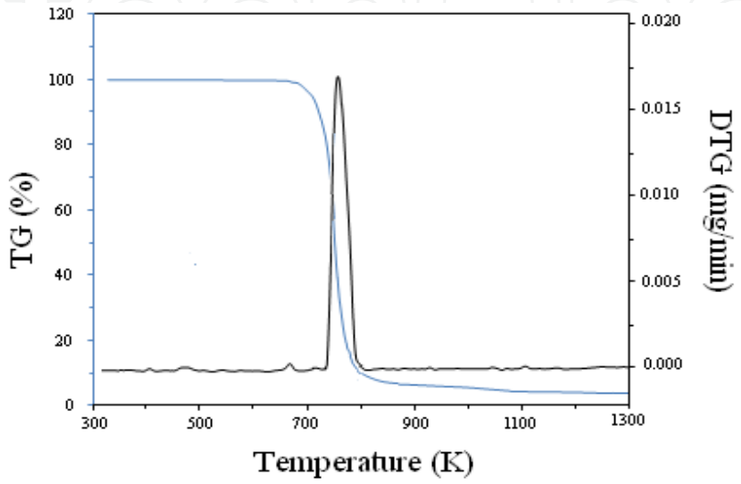

Fig. 16. Thermogravimetric (TG) and thermogravimetric derivative (DTG) curves for: PVP at a heating rate of 10 k/min.

3.5 Determine of optimum parameters of nickel ferrite nanocrystal

To investigate the optimum concentration of PVP in the synthesis of nickel ferrite nanoparticles, we synthesized nickel ferrite nanoparticles with others PVP concentrations of 0, 0.015 and 0.055 gm/ml, and the results are shown in the TEM images in Figure 17 and the FT-IR spectra in Figure 18. Also, optimum temperature for calcinations of nickel ferrite nanoparticle was 723 K because, this temperature was minimum temperature that nanoparticles were pure; furthermore, they have also the lowest particle size with a nearly uniform distribution in shapes.Figure 17a shows that nickel ferrite nanoparticles were formed even in the absence of PVP. However, in this case, it was observed that the nanoparticles did not have a uniform distribution of shapes, and they were aggregated extensively and, in some areas, completely disproportionately distributed. Thus, without the use of PVP in the synthesis of nanoparticles, the small nanoparticles aggregate and produce larger nanoparticles [29] due to high surface energy (as shown earlier in Fig15)

When the concentration of PVP was increased to 0.015 gm/ml, the nickel ferrite nanoparticles that were formed became more regular in shape than in the case without PVP (Figure 17b). But, due to the low concentration of PVP, these nanoparticles also aggregated because there was insufficient PVP to cap them well and prevent their agglomeration.By increasing the PVP concentration to 0.055 gm/ml, the nickel ferrite nanoparticles did not agglomerate, and they were nearly uniform in shape, as shown in Figure 17d. However, in this case, the nickel ferrite nanoparticles ranged in size from 9 to 21 nm, with an estimated

average particle size of 12 nm. These results were similar to the results achieved when a PVP concentration of 0.035 gm/ml was used (shown in Figure 17c). But, due to the high concentration of PVP, traces of organic materials were observed at 1254 cm^{-1}, which was attributed to the C–H bending vibration of methylene groups, as shown in Figure 18b while in concentration of 0.035 gm/mlnickel ferrite nanoparticles were pure (Figure 18a).

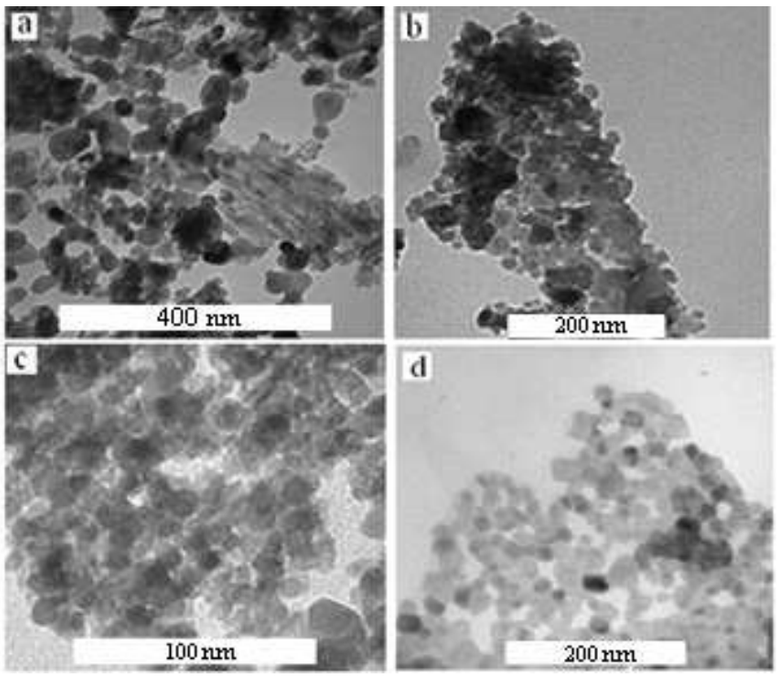

Fig. 17. TEM images of nickel ferrite nanoparticles with PVP concentrations of (a) 0, (b) 0.015, (c) 0.035, and (d) 0.055 gm/ml calcined at 723 K.

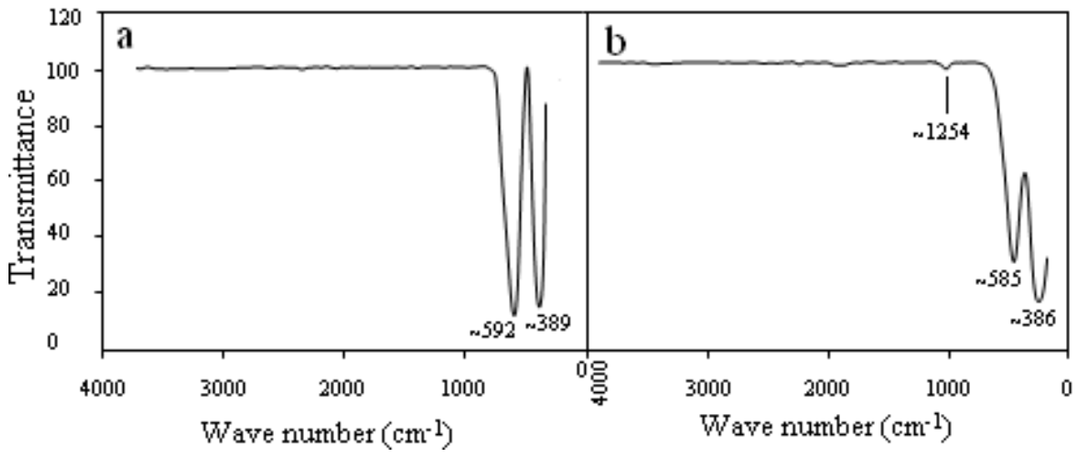

Fig. 18. FTIR spectra of nickel ferrite nanoparticles with PVP concentration of (a) 0.035 and 0.055 gm/ml calcined at 723 K.

So, in fact, it is apparent that the nickel ferrite nanoparticles were contaminated with organic compounds in this case. Therefore, in the thermal treatment method, the optimum concentration of PVP for the synthesis of nickel ferrite nanoparticles is 0.035 gm/ml. That

concentration, in combination with the optimum temperature (723 K) provided the conditions required to fabricate pure nickel ferrite nanoparticles that have the smallest particle size. So, as discussed earlier in connection with Figure 15 and as demonstrated in the above discussion of the results obtained, PVP plays three crucial roles in synthesizing nickel ferrite nanoparticles, i.e., (1) the control of the growth of the nanoparticles; (2) the prevention of agglomeration of the nanoparticles; and (3) the production of nanoparticles that have a uniform distribution of shapes [35].

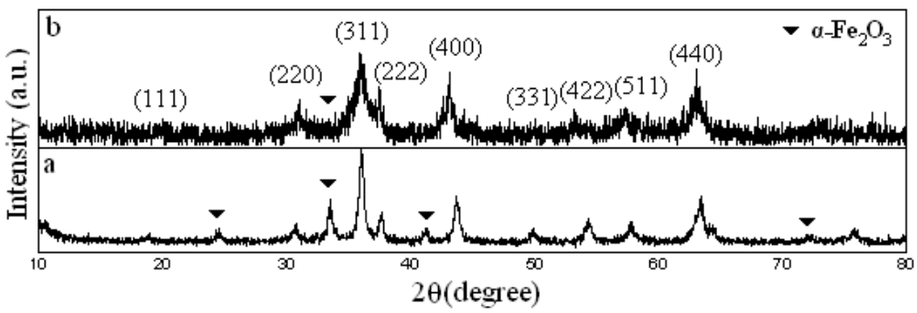

Fig. 19. XRD patterns of nickel ferrite nanoparticles with heating rate of calcination of 10, and 20 K/min calcined at 723.

After our examination, for optimum concentration of PVP (0.035 gm/ml) and optimum temperature for calcinations (723 K) of nickel ferrite nanoparticle, we investigated optimum the time of calcinations and the heating rate of calcinations of nickel ferrite nanoparticles as last optimization.In this investigation, the minimum time that allowed the crystallization to be completed was 3 h as lower than 3 h the crystallization was uncompleted and higher than 3 h particles size increased. The heating rate of calcination was 10 K/min for nickel ferrite nanoparticles calcined at 723K, which was an optimum heating rate. By increasing the heating rate of calcination to 20 K/min, the percent of impure phase of α-Fe_2O_3 increased and the crystallite of nickel ferrite nanoparticles were not as pure as optimum heating rate as shown in Figure19a and Figure 19b.When the heating rate of calcinations was lower than 10 K/min (5 K/min) we wasted long time for calcinations and several neighboring particles fuse together to increase particle sizes by melting their surfaces [36].

Note: We have done exactly these experiments on others ferrites i.e. zinc ferrite and manganese ferrite and have obtained for each of them optimum parameters. But to prevent long or repeated exposures and similar experiments, we reported only the experiments of nickel ferrite nanoparticles and for others ferrites we sufficed only to report of values (Table3).

Pure metal ferrite nanoparticles	Optimum calcinations temperature (K)	Optimum concentration of PVP (gm/ml)	Optimum Heating rate (K/min)	Optimum Calcinations Time (h)
ZnFerrite	873	0.030	10	3
MnFerrite	873	0.030	10	3
NiFerrite	723	0.035	10	3

Table 3. Summary of optimum parameters of metal ferrite nanocrystal prepared by thermal treatment method

3.6 Phase composition and morphology of metal ferrite nanocrystal

XRD and FT-IR were used to characterize the precursors and ferrite nanoparticles calcined at 723, 773, 823 and873 K. The XRD diffraction patterns of the precursor and metal ferrite nanoparticles are shown in Figure20. A broad peak occurred for all samples in the precursor, which does not have sharp diffraction patterns and is still amorphous. The calcined patterns show the reflection planes (111), (220), (311), (222), (400), (331), (422), (511), and (440), which confirm the presence of single-phase in $ZnFe_2O_4$, $MnFe_2O_4$ and $NiFe_2O_4$ with a face-centered cubic structure [37-39].Except for the impure phases of α-Fe_2O_3 (for all the metal ferrite nanoparticles shown in Figure 20a, 20b and 20c) and ZnO (for the zinc ferrite nanopaticles shown in Figure20a), which occur naturally as hematite and zincite, respectively [37, 40], the remaining peaks correspond to the standard pattern of $ZnFe_2O_4$ (cubic, space group: Fd3m, Z = 8; ICDD PDF: 22-1012), $MnFe_2O_4$ (cubic, space group: Fd3m, Z = 8; ICDD PDF: 73-1964) and $NiFe_2O_4$ (cubic, space group: Fd3m, Z = 8; ICDD PDF: 44-1485)[37-39].

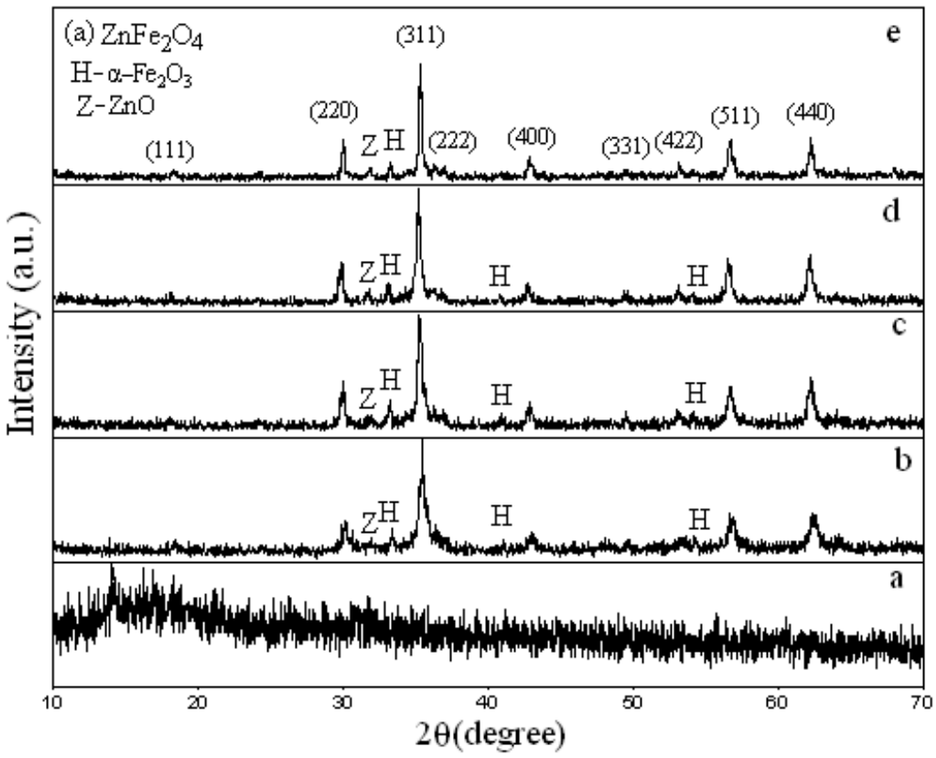

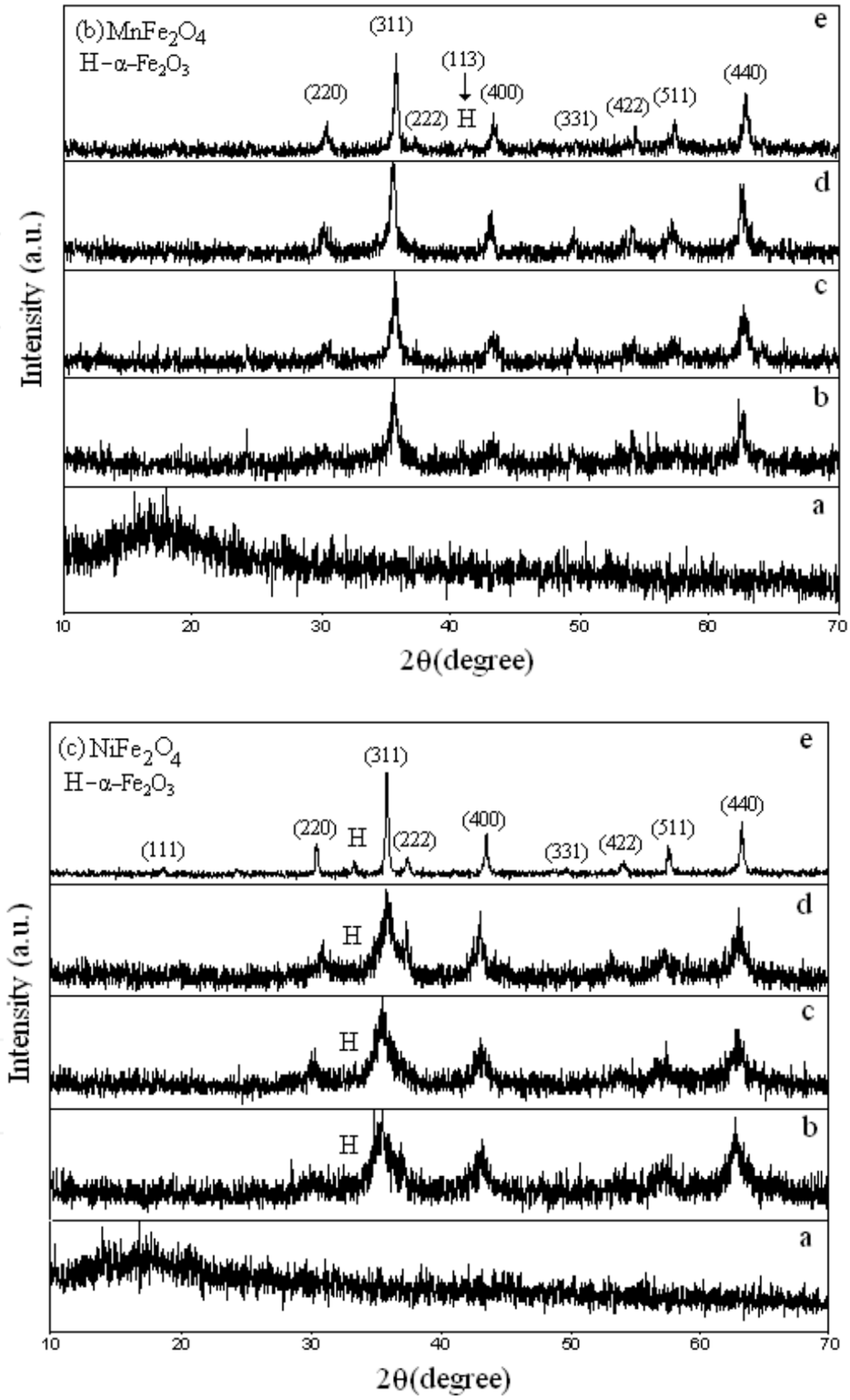

Fig. 20. XRD patterns of precursors and metal ferrite nanoparicles of (a) $ZnFe_2O_4$, (b) $MnFe_2O_4$ and (c) $NiFe_2O_4$ calcined at 723, 773, 823 and 873 K.

The results obtained from XRD were analyzed using the Chekcell program, which calculated lattice parameters of the samples calcined at 723, 773, 823, and 873 K (Table 4). XRD results were analyzed by the Scherer formula:

$$D=0.9\lambda/(\beta\cos\theta), \quad (4)$$

where D is the crystallite size (nm), β is the full width of the diffraction line at half the maximum intensity measured in radians, λ is X-ray wavelength, and θ is the Bragg angle [41]. This formula was used to estimate the average particle sizes, which ranged in Table 4.

Specimens $MeFe_2O_4$	Calcination temperature (K)	Average particle size XRD (nm)	Average particle size TEM (nm)	Lattice Parameter (nm)	Saturation magnetization M_s (emu/g)	Coercivity field H_c (Oe)
ZnFerrite 1	723	21	17±7	0.8498	4.49	negligible
ZnFerrite 2	773	24	22±2.5	0.8468	2.66	negligible
ZnFerrite 3	823	31	27±5	0.8471	1.81	negligible
ZnFerrite 4	873	33	31±11	0.8479	0.74	negligible
MnFerrite 1	723	15	12±4	0.8524	3.06	negligible
MnFerrite 2	773	17	15±2	0.8577	6.31	negligible
MnFerrite 3	823	20	17±5	0.8558	7.96	negligible
MnFerrite 4	873	23	22±4	0.8537	15.78	negligible
NiFerrite 1	723	15	12±3	0.8368	21.37	150(-148)
NiFerrite 2	773	27	22±12	0.8373	26.67	107(-112)
NiFerrite 3	823	51	47±11	0.8418	29.05	51(-43)
NiFerrite 4	873	69	67±8	0.8402	34.19	32(-38)

Table 4. Summery of variation of particle sizes, lattice parameters, saturation magnetization and coercivity field with temperature calcinations for metal ferrite nanoparticles calcined at 723, 773, 823 and 873 K.

Figure 21 shows the FT-IR spectrum of the precursor and calcined samples in the wave-number range between 280 and 4000 cm^{-1}.The IR spectra of all calcined samples show the two principle absorption bands in the range of 300-600 cm^{-1} .These two vibration bands Fe↔O and M↔O are corresponded to the intrinsic lattice vibrations of octahedral and tetrahedral coordination compounds in the spinel structure, respectively [42].The bands with peaks around 670 and 850 cm^{-1} were assigned to the formation vibration of C-N=O bending and the C-C ring. The bands in the range of 1200 to 1250 cm^{-1} was associated with C-N stretching vibration, and the appearance of the bands in the range of 1350 to 1450 cm^{-1} was attributed to C-H bending vibration from the methylene groups. Finally, there were bands in the region 1600 to1800 cm^{-1} and around 3400 to 3500 cm^{-1}, which were associated with C=O stretching vibration and N-H or O-H stretching vibration, respectively [43].

The vibrational spectra of the absorption bands of pure $ZnFe_2O_4$ and $MnFe_2O_4$ nanoparticles were observed at 388, and 541 cm^{-1}, and at 404, 502, and 556 $cm^{-1}$for the samples calcined at 873 K (shown in Figure 21a and 21b). In these two ferrite nanoparticles, at the lower temperature of 873 K, however, there was still traces of broadband absorption peaks at 1497,

1761 and 3504 cm^{-1} due to traces of adsorbed or atmospheric CO_2 and O-H stretching vibration, respectively while in $NiFe_2O_4$ nanoparticles (Figure 21c), at the lower temperature of 723 K, there was still a trace of a broadband absorption peaks due to ester formation as consequence of the scission of the CO_2 and O-H stretching vibration(This is not shown in the Figure21). This suggests that, in thermal treatment method, the calcination temperature of pure nickel ferrite nanoparticles is lower than pure zinc and manganese ferrite nanoparticles [35,44,45].This IR analysis was very useful for establishing the calcination temperature because it removed unwanted ions that may pollute the crystal lattice during preparation.

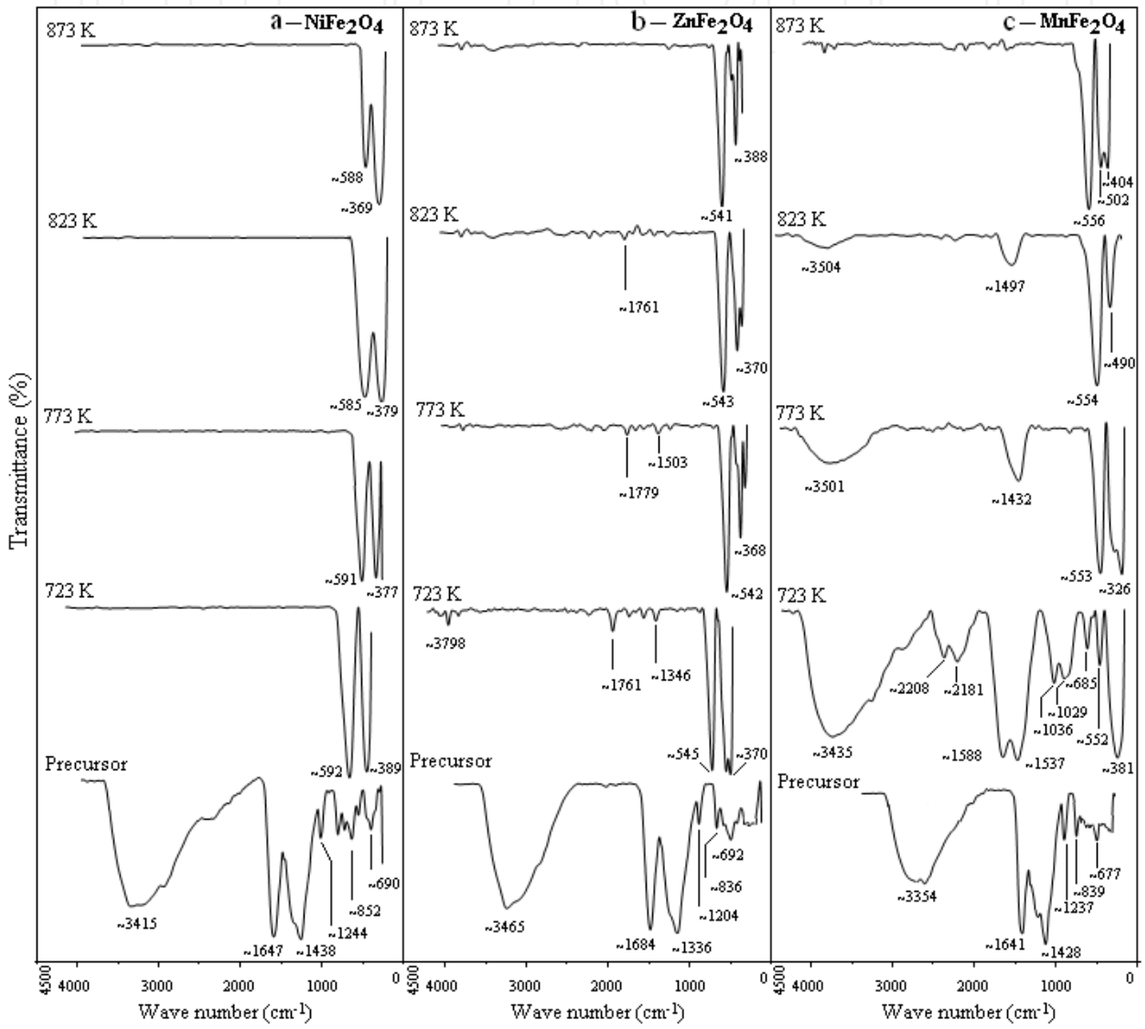

Fig. 21. FT-IR spectra of precursors and metal ferrite nanoparicles of (a) ZnFe2O4, (b) $MnFe_2O_4$ and (c) $NiFe_2O_4$ calcined at 723, 773, 823 and 873 K.

The TEM images (Figures 22-24) show the size, shape, and distribution of $ZnFe_2O_4$, $MnFe_2O_4$ and $NiFe_2O_4$ nanoparticles at different calcination temperatures from 723 to 873 K. The results indicate that the samples prepared by the thermal treatment method were uniform in morphology and particle size distribution. The average particle size of the $ZnFe_2O_4$, $MnFe_2O_4$ and $NiFe_2O_4$ nanoparticles were determined by TEM which increased

with the calcinations temperature and they had good agreement with XRD results (Table 4).This suggested that several neighboring particles fused together to increase the particle size by the melting of their surfaces [46]. Particle size enlargement due to grain growth has been observed previously in zinc.manganese and nickel ferrite systems at higher calcination temperatures [35,44,45].

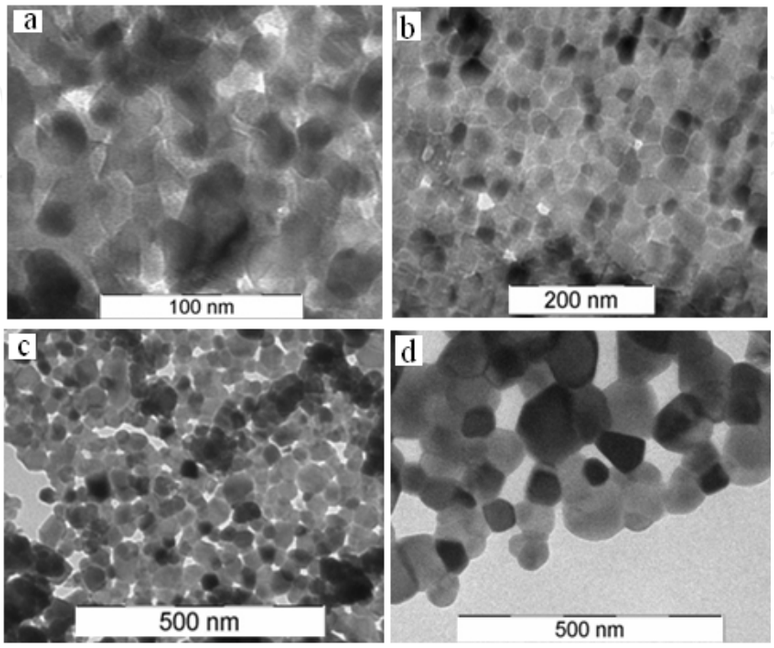

Fig. 22. TEM images of zinc ferrite nanoparticles calcined at (a) 723 (b) 773 (c) 823 (d) 873 K.

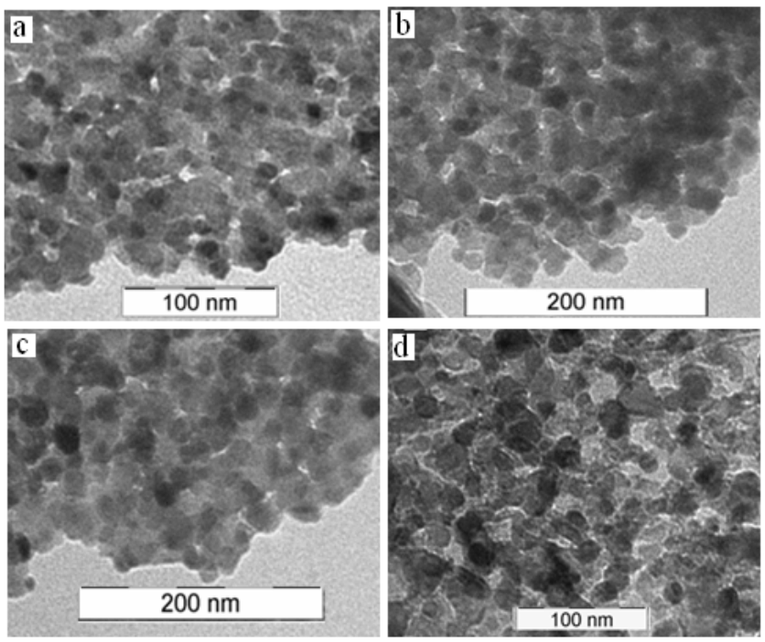

Fig. 23. TEM images of manganese ferrite nanoparticles calcined at (a) 723 (b) 773 (c) 823 (d) 873 K.

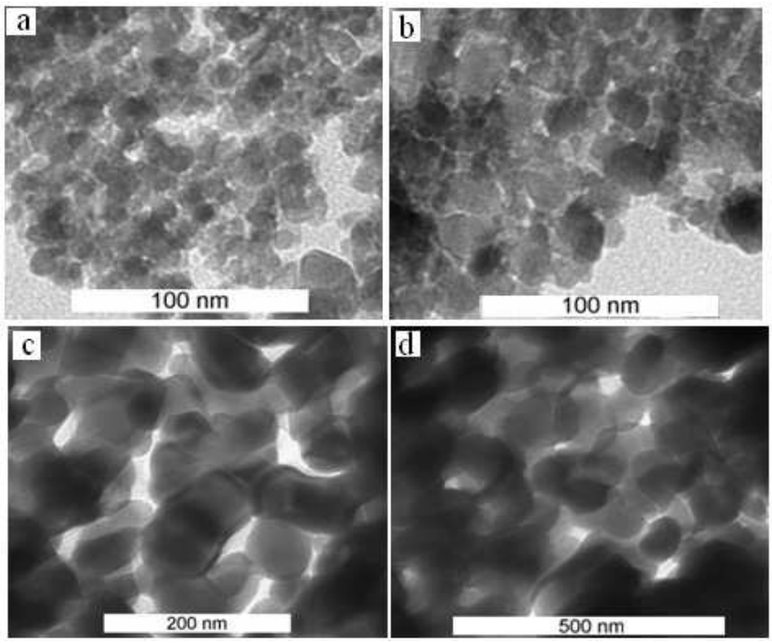

Fig. 24. TEM images of nickel ferrite nanoparticles calcined at (a) 723 (b) 773 (c) 823 (d) 873 K.

3.7 Magnetic properties of MFe_2O_4 nanocrystal obtained VSM

The room temperature (300 K) magnetic properties of the prepared precursors and MFe_2O_4 nanoparticles calcined at different temperatures were investigated by the VSM technique in the range of approximately –15 to +15 kOe. Except for the precursors which were non-magnetic material, the calcined samples exhibited different magnetic behaviors. The room temperature magnetic behaviors of metal ferrite nanoparticles which fabricated by thermal treatment method, can be explained as the results of the four important factors: cationic distribution in spinel structure, the heating rate of calcinations, impurity phase of α-Fe_2O_3, and the surface spin structure of nanoparticles. Although all of these factors can be effective in magnetic behaviors but, their effects on the ferrite nanoparticles with different structures are not similar. We will have a discussion on this matter in next subsections.

3.7.1 Znic ferrite nanoparticles

Figure 25 shows the magnetization curves of precursor and $ZnFe_2O_4$ nanoparticles at (a) 723 (b) 773 (c) 823 and (d) 873 K. Their coercivity fields (H_c) are almost negligible, and all of them exhibit super-paramagnetic behaviours. Table 4 provides the values of saturation magnetization (M_s) of the calcined samples, along with calcinations temperatures and particle sizes. These data make it clear that different parameters were responsible for the saturation magnetization decreasing from 4.49 to 0.74 emu/g when the particle size increased from 17 to 31 nm. Cation inversion is one of the most important parameters that can be effective in the variation of the magnetic properties of zinc ferrite nanoparticles from the properties of the bulk form of the same material. In bulk form, zinc ferrite has an normal spinel structure in which all Zn^{2+} ions are in A sites and Fe^{3+} ions are distributed in B sites [47]. However, in bulk, zinc ferrite only occurs in intra-sub-lattice (B-B) exchange

interactions, and it does not have intra-sub-lattice (A-A) exchange interactions or inter-sub-lattice (A-B) super-exchange interactions [48]. Inter-sub-lattice (A-B) super-exchange interactions of the cations are much stronger than the (A-A) and (B-B) interactions [18].Due to the cation inversion, which originates from thermal and mechanical treatment [40], the structure of $ZnFe_2O_4$ transfers from a normal spinel structure to a mixed spinel structure [48]. This cation inversion causes the zinc ferrite nanoparticles to experience inter-sub-lattice (A-B) super-exchange interactions and intra-sub-lattice (A-A) exchange interactions in addition to intra-sub-lattice (B-B) exchange interactions. But, due to the degree of inversion, which is large for smaller size particles, inter-sub-lattice (A-B) super-exchange interactions in smaller size particles occur to a greater extent than in larger size particles. Hence, saturation magnetization increases for smaller size particles [49], using Mossbauer's experiment, showed that the degree of inversion is large in the case of smaller size particles. Also, an impure α-Fe_2O_3 phase was detected by XRD (Figure20a), the heating rate of calcinations and the surface spin structure can be an influence that increases the saturation magnetization in smaller size particles [37].

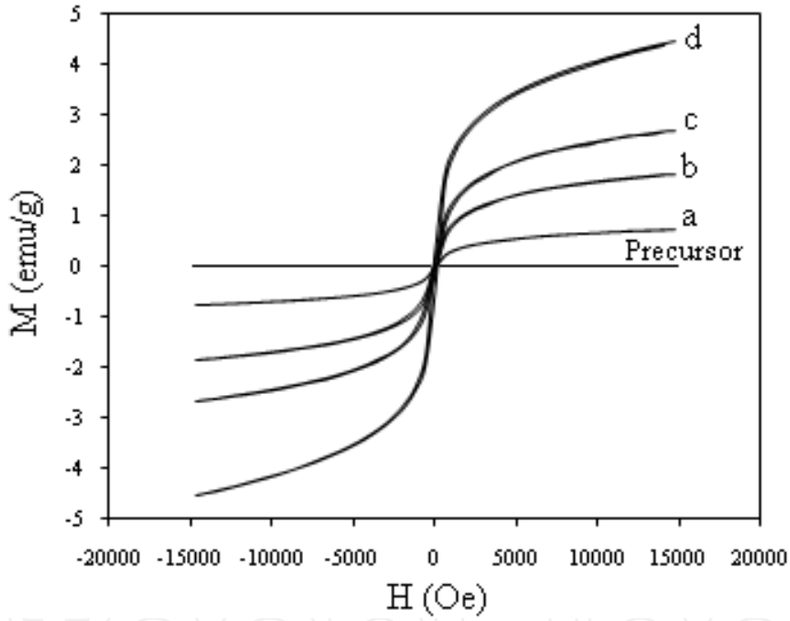

Fig. 25. Magnetization curves at room temperature for precursor and zinc ferrite nanoparticles calcined at (a) 723 (b) 773 (c) 823 (d) 873 K.

3.7.2 Manganese ferrite nanoparticles

Figure 26 shows the curves of magnetization of precursor and $MnFe_2O_4$ nanoparticles which exhibited a typical super-paramagnetic behavior. Table 4 depicts the values of saturation magnetization (M_s) of different samples. When the calcination temperature increased from 723 K to 873 K, the saturation magnetization increased from 3.06 to 15.78 emu/g. This can be attributed to spin canting and surface spin disorder that occurred in these nanoparticles [50].The interactions between the A and B sub-lattices in the spinel lattice system (AB_2O_4) consist of inter-sub-lattice (A-B) super-exchange interactions and intra-sub-lattice (A-A) and (B-B) exchange interactions. Inter-sub-lattice super-exchange interactions of the cations on the

(A-B) are much stronger than the (A-A) and (B-B) intra-sub-lattice exchange interactions [18, 51].As discussed earlier (Figure20b), by increasing the calcination temperature of the $MnFe_2O_4$ nanoparticles, Fe^{3+} ions transferred from B site to A site, so, consequently, the accumulation of Fe^{3+} ions increased in A site; however, the Fe_A^{3+}- Fe_B^{3+} super-exchange interactions increased (Fe_A^{3+}- Fe_B^{3+} interactions were twice as strong as the Mn_A^{2+}- Fe_B^{3+} interactions), and this can lead to an increase in saturation magnetization in $MnFe_2O_4$ nanoparticles [52]. Aslibeiki *et al*. [53] showed that saturation magnetization increases with increasing temperature and particle size in $MnFe_2O_4$ nanoparticles.It has been reported [54] that the spin disorder may occur on the surface of the nanoparticles as well as within the cores of the nanoparticles due to vacant sub-lattice disorder sites (Fe_A^{3+}) and poor crystal structure. The other point that is understood from Table 4 is that the values of saturation magnetization are expressively lower than those reported for the bulk $MnFe_2O_4$ (80 emu/g) [55]. The decrease in saturation magnetization of all the samples compared to that of the bulk is ascribed to the surface effects in these nanoparticles. The existence of an inactive magnetic layer or a disordered layer on the surfaces of the nanoparticles and the heating rate of calcinations can be due to the decrease of saturation magnetization compared to the bulk value [56, 57].

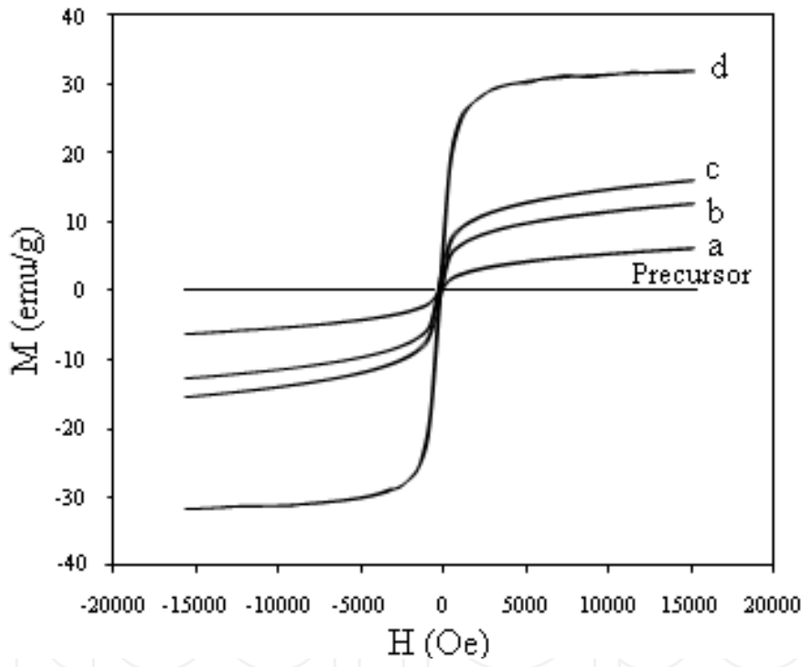

Fig. 26. Magnetization curves at room temperature for precursor and manganese ferrite nanoparticles calcined at (a) 723 (b) 773 (c) 823 (d) 873 K.

3.7.3 Nickel ferrite nanoparticles

Figure 27 (left) exhibits the hysteresis curves of precursor and $NiFe_2O_4$ nanoparticles which exhibited a typical ferromagnetic behavior. It can be seen from this figure that the magnetic properties of nanoparticles depended on the calcinations temperature. Saturation magnetization (M_s) values of 21.37, 26.67, 29.05 and 34.19 emu/g are observed for the nickel ferrite nanoparticles calcined at 723, 773, 823, and 873 K, respectively. There is a clear tendency of M_s increase with the enhancement of crystallinity of the $NiFe_2O_4$ nanoparticles.

As listed in Table 4, the values of M_s for the nickel ferrite nanoparticles were observed to increase with increasing temperature [58, 59]. The largest saturation magnetization was 34.19 emu/g for the sample calcined at 873 K, which is lower than that reported for the multi-domain, bulk nickel ferrite (55emu/g) [60].The decrease in saturation magnetization of these samples, compared to that of bulk material, depends on four factors explained in section 2.15. It seems that in inversed spinel ferrite nanoparticles such as nickel ferrite or cobalt ferrite nanoparticles which fabricated by thermal treatment method, the heating rate of calcination is more important than other parameters that can effectively increase or decrease the saturation magnetization.[35,61]. In our experiments, the heating rate of calcination was 10 K/min for nickel, zinc and manganese ferrite nanoparticles calcined at 723, 773, 823, and 873 K, which was a medium heating rate (Table 3). Therefore, it is possible that calcination at a slower heating rate would allow crystallization to be more complete and the magnetic phase could also increase, resulting in larger saturation magnetization. Sangmanee *et al*. [36] showed that saturation magnetization increases from 9.7 to 56.5 emu/g with decreasing the heating rate of calcination from 20 K/min to 5 K/min in cobalt ferrite nanostructures calcined at 773 K and fabricated by electrospinning. In addition, the appearance of the weakly-magnetic, impure phase of α-Fe_2O_3 (shown in Figure20c) can reduce the saturation magnetization [37].Variations of saturation magnetization with particle size for nickel ferrite nanoparticles are listed in Table 4. The saturation magnetization values of the calcined samples increase with increasing particle size, which may be attributed to the surface effects in these nanoparticles. The surface of the nanoparticles seems to be composed of some distorted or slanted spins that repel the core spins to align the field direction. Consequently, the saturation magnetization decreases for smaller sizes [62-64]. Furthermore, the surface is likely to behave as an inactive and dead layer with inconsiderable magnetization [56, 57]. The variation in the value of the saturation magnetization with particle size also can be resulted from the cation redistribution (interchanging of Ni and Fe ions of the tetrahedral and octahedral sites). This cation redistribution, causes that the structure of $NiFe_2O_4$ transfers from an inverse spinel structure

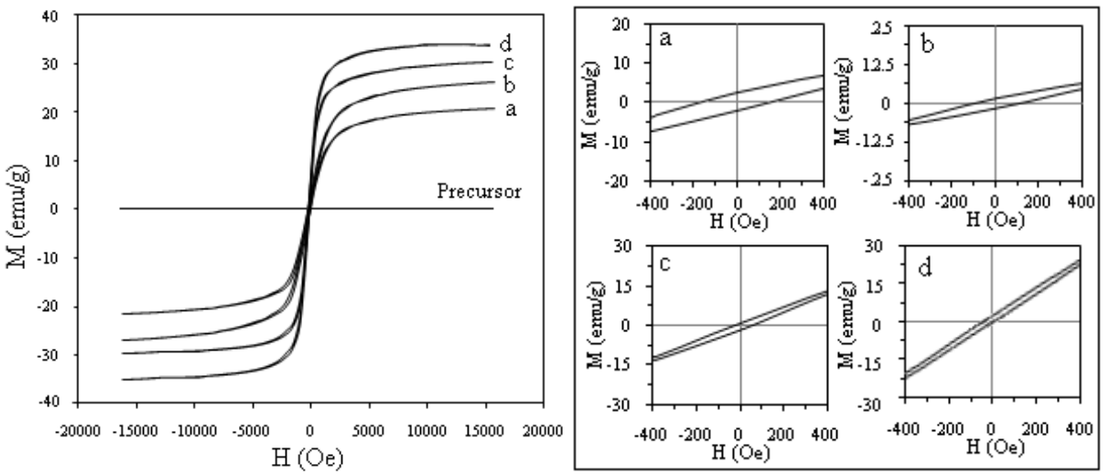

Fig. 27. (left) The magnetization curves of precursor and the nickel ferrite nanoparticles calcined at (a) 723 (b) 773 (c) 823 and (d) 873 K which measured at room temperature in the range of approximately −15 to +15 kOe. Figure27. (right) the expanded field region around the origin for clear visibility of the readers, in the range of approximately −400 to +400 Oe.

to a mixed spinel structure [65].Figure 27 (right) shows the expanded coercivity field (H_c) of region around of origin for clear visibility at room temperature in the range of approximately –400 to +400 Oe. The coercivity field values are listed in Table 4. These variations are not similar with saturation magnetization because, when the particle size increases from 15 to 69 nm, the coercivity field decreases from 150 to 32 Oe at room temperature. Variations of the coercivity field with particle size of nickel ferrite nanoparticles can be elucidated on the basis of domain structure, critical size, and the anisotropy of the crystal [16, 66-67].

Finaly, It is worth noting that the magnetic properties of similar ferrite nanoparticles of the same particle size differ depending on the preparation method used. Table 5 shows some literature values of M_s and H_c that were measured at similar conditions for some spinel ferrite nanoparticles. The data show that the pairs of similar spinel ferrite nanoparticles of the same particle size have different saturation magnetization values and coercivity fields. The results indicate that, in fact, the magnetic properties of ferrites are related primarily to the methods used to prepare them.

Specimens	Preparation method	Average particle size (nm)	Saturation magnetization Ms (emu/g)	Coercivity field Hc (Oe)	References
ZnFerrite	Combustion	20	4	Negligible	[68]
ZnFerrite	Modified sol	~20	1.4	156	[37]
NiFerrite	gel	~9	32.1	59	[69]
NiFerrite	Sol gel	9	11.9	Negligible	[70]
CoFerrite	Coprecipitation	30	77	2000-2700	[71]
CoFerrite	Mechanic alloying	30	30	Negligible	[72]
	Hydrothermal				

Table 5. Magnetic properties of some spinel ferrite nanoparticles reported in the literatures which were measured at room temperature in range of approximately −10 to +10 kOe.

4. Conclusion

We have succeeded in fabricating spinel ferrite nanoparticles such as zinc ferrite ($ZnFe_2O_4$), manganese ferrite ($MnFe_2O_4$) and nickel ferrite ($NiFe_2O_4$) nanocrystals by a thermal treatment method utilizing only metal nitrates and as precursors, deionized water as a solvent and PVP as a capping agent.PVP played three crucial roles in synthesizing spinel ferrite nanoparticles, i.e., (1) the control of the growth of the nanoparticles; (2) the prevention of agglomeration of the nanoparticles; and (3) the production of nanoparticles that have a uniform distribution of shapes. The average particle sizes of metal ferrite nanoparticles were determined by TEM which increased with the calcinations temperature and they had good agreement with XRD results. FT-IR confirmed the presence of metal oxide bands at all temperatures and the absence of organic bands at 873 K for zinc and manganese ferrite nanoparticles and at 723 K for the nickel ferrite nanoparticles.VSM results demonstrated that zinc and manganese ferrite nanoparticles displayed super paramagnetic behaviors while nickel ferrite nanoparticles exhibited ferromagnetic behaviors. The present

study also substantiated that, in ferrites, the values of the quantities that were acquired by VSM, such as saturation magnetization and coercivity field, are primarily dependent on the methods of preparation of the ferrites. This simple method, which is cost-effective and environmentally friendly, produces no toxic byproducts and can be used to fabricate pure, crystalline spinel metal ferrite nanocrystals.

Furthermore, this method can be extended to the synthesis of other spinel ferrite nanoparticles of interest.

5. References

[1] Gubin, S.P., Koksharov, Yu. A., Khomutov, G.B., Yurkov, G.Yu. (2005).Magnetic nanoparticles: preparation, structure and properties. Russian Chemical Reviews (74) 489 – 520.
[2] Baraton, M I. (2002).Synthesis, Functionalization, and Surface Treatment of Nanoparticles. University of Limoges, Franch.
[3] Callister, W. (2003). Materials science and engineering an introduction. Sixth ed. New York: JoHn Wiley & Sons, Inc.
[4] Spaldin, N. (2003). Magnetic materials: Fundamentals and device aplications. Cambridge: Cambridge University press.
[5] Goldman, A. (1990).Modern Ferrite Technology. Van Nostrand Reinhold, New York.
[6] Tilley, R.J.D (2004). Understanding solids: the science of materials. John Wiley and Sons, p 376.
[7] Winkler,G.(1971). Crystallography, chemistry and technology of ferrites; in: Magnetic properties of Materials, ed. J Smit, New York, McGraw-Hill.
[8] Bragg, W. H. (1915 a), Nature 95, 561.
[9] Bragg, W. H. (1915 b), Phil. Mag. 30, 305.
[10] Mehdiye, T.R., Gashimov, A.M., and Habibzade, A.A., (2008). Electromagnetic Processes in frequency-dependent resistor sheath.Fizika Cild Xiv №3 p 80-88.
[11] Gorter, E. W. (1954), Philips Res. Rep. 9, 321.
[12] Daliya S. M., and Juang, R. S. (2007). An overview of the structure and magnetism of spinel ferrite nanoparticles and their synthesis in microemulsions.Chemical Engineering Journal, 129 (1-3): 51–65.
[13] Stoner, E.C., Wohlfarth, E. P. (1948). A mechanism of magnetic hysteresis in heterogeneous alloys. IEEE Transactions on Magnetics, 27 (4): 3475 – 3518.
[14] Jiles, D. (1991). Introduction to Magnetism and Magnetic Materials. (First ed) Londond: Chapman & Hall.
[15] Bozorth, R. M. (1993). Ferromagnetism. Editorial Board ,New York.
[16] Cullity, B. D. (1978). Introduction to Magnetic Materials (2nd ed.). Addison-Wesley Publishing.
[17] Cao, X., and Gu, L. (2005). Spindly cobalt ferrite nanocrystals: preparation, characterization and magnetic properties. Nanotechnology, 16 (2): 180-185.
[18] Atif, M., Hasanian, S. K., and Nadeem, M. (2006). Magnetization of sol-gel prepared zinc ferrite nanoparticles: Effects of inversion and particle size. Solid State Communications, 138(8): 416-421.
[19] Jiang, J.Z., Wynn, P., Morup, S., Okada, T., and Berry, F.J. (1999). Nanostructured Materials, 12(5): 737-740.

[20] Shenoy,S.D., Joy, P.A., M.R. Anantharaman (2004). Effect of mechanical milling on the structural, magnetic and dielectric properties of coprecipitated ultrafine zinc ferrite Journal of Magnetism and Magnetic Materials (269) 217-226.

[21] Zhang,D.E. Zhang,X.J. Ni, X.M. Zheng, H.G. and Yang, D.D. (2005) Design and experiment of the self-propelled combine harvester for corn and stalk, J. Magn. Magn. Mater. (292 79-82.

[22] Li, H., Wu, H.Z., Xiao,G.X. (2010). Effects of synthetic conditions on particle size and magnetic properties of NiFe2O4, Powder Technol. (198) 157-166.

[23] Kale, A. Gubbala, S. R. Misra, D.K. (2004). Magnetic behavior of nanocrystalline nickel ferrite synthesized by the reverse micelle technique, J. Magn. Magn. Mater. (277) 350-358.

[24] Hochepied, J.P. Bonville, J.F., and Pileni, M.P.(2000). Non stoichiometric Zinc Ferrite nancrystals: Syntheses and magnetic properties J. Phys. Chem.; (104) 905-912.

[25] Sivakumar, P., Ramesh, R., Ramanand , A., Ponnusamy, S., and Muthamizhchelvan, C. (2011). Synthesis and characterization of NiFe2O4 nanosheet via polymer assisted co-precipitation method. Material. Letters, 65(3): 483-485.

[26] Koebel, M. M., Louis, C., Jones, and Gabor, A.S. (2008). Preparation of size-tunable, highly monodisperse PVP-protected Pt-nanoparticles by seed-mediated growth. Journal of Nanoparticle Research, 10(6): 1063-1069.

[27] Roosen, A.R., Carter. W.C. (1998). Simulations of microstructural evolution: Anisotropic growth and coarsening. Physica A, 261(1): 232-247.

[28] Ghosh, G., Naskar, M. K., Patra, A., and Chatterjee, M. (2006). Synthesis and characterization of PVP-encapsulated ZnS nanoparticles. Optical Materials 28(8-9): 1047-1053.

[29] Shao, H., Y. H., H. Lee, Y. J. Suh , C. O. Kim. (2006). Effect of PVP on the morphology of cobalt nanoparticles prepared by thermal decomposition of cobalt acetate. Current Applied Physics, 6(S1): e195-e197.

[30] Wen-yao, H., Guo.-cai, X. (2010). Characterization of nano-Ag/PVP composites synthesized via ultra-violet irradiation Journal of coal Science and Engineering, 16(2): 188-192.

[31] Tsuji, M., Hashimoto, M., Nishizawa, Y., and Tsuji, T. (2004). Synthesis of gold nanorods and nanowires by microwave-polyol method. Materials. Letters, 58(17-18): 2326-2330.

[32] Kumar, S.V., Musturappa, T.E., Prasannakumar, S., Mahadevan, K.M., Sherigara, B.S. (2007). N-Vinylpyrrolidone and ethoxyethyl methacrylate copolymer: synthesis, characterization and reactivity ratios. Journal of Macromolecular Science, Part A: Pure and Applied Chemistry, 44(11), 1161–1169.

[33] Lau, C., Mi, Y. (2002). A study of blending and complexation of poly (acrylic acid)/poly(vinyl pyrrolidone). Polymer, 43(3): 823–829.

[34] Silva, M.F., Silva,C.A., Fogo,F.C., Pineda,E.A.G., and Hechenleitner A.A.W. (2005). Thermal and FTIR study of polyvinylpyrrolidone/lignin blends. Journal of Therml Analysis and Calorimetry, 79(2): 367–370.

[35] Naseri, M. G. Saion, E.B. Abbastabar Ahangar, H. Hashim, M. and Shaari, A. H.(2011) Simple preparation and characterization of nickel ferrite nanocrystals by a thermal treatment method. Powder Technology 212, 80–88.

[36] Sangmanee, M., and Maensiri, S. (2009). Nanostructures and magnetic properties of cobalt ferrite ($CoFe_2O_4$) fabricated by electrospinning. Applied Physics A, 97(1): 167-177.

[37] Laokul, P., Amornkitbamrung, V., Seraphin ,S., and Maensiri, S. (2011). Characterization and magnetic properties of nanocrystalline $CuFe_2O_4$, $NiFe_2O_4$, $ZnFe_2O_4$ powders prepared by the Aloe vera extract solution. Current Applied Physics, 11(1): 101-108.

[38] L. Zhen, K. He, C.Y. Xu, W.Z. Shao (2008). Synthesis and characterization of single-crystalline $MnFe_2O_4$ nanorods via a surfactant-free hydrothermal route. Journal of Magnetism and Magnetic Materials 320 (2008) 2672– 2675.

[39] S. Bid, P. Sahu, S.K. Pradhan.(2007) Microstructure characterization of mechanosynthesized nanocrystalline $NiFe_2O_4$ by Rietveld's analysis. Physica E (39) 175–184.

[40] Singh, J. P., Srivastava, R. C., Agrawal, H. M., Kumar, R. (2010). Magnetic behaviour of nanosized zinc ferrite under heavy ion irradiation.Nuclear Instruments and Methods in Physics Research Section B: Beam Interactions with Materials and Atoms, 268(9): 1422-1426.

[41] B.D. Cullity, Elements of X-ray Diffraction, (2nd ed.), Addison-Wesley, London,1978, p.102.

[42] R.K. Selvan, C.O. Augustin, L.B. Berchmans, R. Sarawathi, (2003).Combustion synthesis of $CuFe_2O_4$ Mater. Res. Bull. (38) 41-45.

[43] M.I. Lorı´a-Bastarrachea,W. Herrera-Kao, J.V. Cauich-Rodrı´guez, J. M. Cervantes-Uc, H. Va´zquez-Torres, A.A vila-Ortega, J. Therm. Anal. Calorim. DOI 10.1007/s10973-010-1061-9, 2010

[44] Naseri , M. G. Saion,E. B. Ahangar, H. A. Hashim, M. Shaari, A.H. (2011) Synthesis and characterization of manganese ferrite nanoparticles by thermal treatment method. Journal of Magnetism and Magnetic Materials, (323) 1745-1749.

[45] Naseri , M. G. Saion,E. B. Hashim, M. Shaari, A. H. Ahangar, H. A. (2011). Synthesis and characterization of zinc ferrite nanoparticles by a thermal treatment method. Solid State Communications 151 (2011) 1031–1035.

[46] Qu, Y., Yang, Haibin, Yang, N., Fan, Y., Zhu, H., and Zou,G. (2006). The effect of reaction temperature on the particle size, structure and magnetic properties of coprecipitated $CoFe_2O_4$ nanoparticles. Materials. Letters, 60(29-30): 3548-3552.

[47] Mathew, D.S., and Juang, R. S. (2007). An overview of the structure and magnetism of spinel ferrite nanoparticles and their synthesis in microemulsions. Chemical Engineering Journal, 129(1-3): 51-65.

[48] Li, F.S., Wang, L., Wang, J.B., Zhou, Q.G., Zhou, X.Z., Kunkel, H.P., and Williams, G. (2004). Site preference of Fe in nanoparticles of ZnFe2O4. Journal of Magnetism and Magnetic Materials, 268(3): 332-339.

[49] Roy, M.K., Haldar, B., and Verma, H. C. (2006). Characteristic length scales of nanosize zinc ferrite. Nanotechnology, 17(1): 232-237.

[50] Gu, Z., Xiang, X., Fan, G., and Li, Feng. (2008). Facile synthesis and characterization of cobalt ferrite nanocrystals via a simple reduction-oxidation route. Journal of Physical Chemistry C, 112(47): 18459-18466.

[51] Ammar, S., Jouini, N., Fiévet, F., Beji, Z., Smiri, L., Moliné,P., Danot, M., and Grenèche, J.M. (2006). Magnetic properties of zinc ferrite nanoparticles synthesized by hydrolysis in a polyol medium. Journal of Physics: Condensed Matter, 18(39): 9055-9069.

[52] Jianjun, L., Hongming, Y., Guodong, L., Liu, Yanju, and Leng, J. (2010). Cation distribution dependence of magnetic properties of sol-gel prepared $MnFe_2O_4$ spinel ferrite nanoparticles Journal of Magnetism and Magnetic Materials,322(21): 3396-3400.

[53] Aslibeiki, B., H. Salamati, P. K., Eshraghi, M., and Tahmasebi, T. (2010). Superspin glass state in $MnFe_2O_4$ nanoparticles. Journal of Magnetism and Magnetic Materials, 322(19): 2929-2934.

[54] Morales,M.P., Veintemillas-Verdaguer, S., Montero, M.I., and Serna, C.J. (1999). Surface and Internal Spin Canting in γ-Fe_2O_3 Nanoparticles. Chemistry of. Materials, 11(11): 3058.

[55] Brabers, V. A. M. (1995). In Handbook of Magnetic Materials (Vol. 8). New York.

[56] Nogues, J., Sort, J., Langlias, V., Skumryev, V., Suriñach, S., Muñoz, J.S., and Baró, M.D. (2005). Exchange bias in nanostructures. Physics Reports, 422(3): 65-117.

[57] Maaz, K., Mumtaz, A., Hasanain, S.K., and Ceylan, A. (2007). Synthesis and magnetic properties of cobalt ferrite ($CoFe_2O_4$) nanoparticles prepared by wet chemical route. Journal of Magnetism and Magnetic Materials, 308(2): 289-295.

[58] Hanh, N., Quy, O. K., Thuy, N.P., Tung, L.D., and Spinu, L. (2003). Synthesis of cobalt ferrite nanocrystallites by the forced hydrolysis method and investigation of their magnetic properties. Physica B:Condensed Matter, 327(2-4): 382-384.

[59] Maensiri, S., Masingboon, C., Boonchom, B., and Seraphin, S. (2007). A simple route to synthesize nickel ferrite ($NiFe_2O_4$) nanoparticles using egg white. Scripta Materialia, 56(9): 797-800.

[60] Smit, J., and Wijn, H. P. J. (1959). Ferrites-physical properties of ferromagnetic oxides in relation to their technical applications. New York: Wiley.

[61] Naseri, M. G., Saion, E. B., Ahangar, H. A., Shaari, A. H. and Hashim, M.(2010). Simple Synthesis and Characterization of Cobalt Ferrite Nanoparticles by a Thermal TreatmentMethod Journal of Nanomaterials (2010) 1-8.

[62] Berkowitz, A.E., Lahut, J. A., and VanBuren, C.E. (1980). Properties of Magnetic Fluid Particles. IEEE Transactions on Magnetics, MAG-16(2): 184-190.

[63] Berkowitz, A.E., Lahut, J. A., Jacobs, I.S., Levinson, L.M., and Forester, D.W. (1975). Spin pinning at ferrite-organic interfaces. Physical Review Letters, 34(10): 594-597.

[64] Coey, J. M. D. (1971). Noncollinear spin arrangement in ultrafine ferrimagnetic crystallites. Physical. Review. Letters, 27(17): 1140-1142.

[65] Jacob, J., and Khadar., M. A. (2010). Investigation of mixed spinel structure of nanostructured nickel ferrite. Journal of. Applied. Physics 107(11): 114310-114320.

[66] Hadjipanayis, G.C., and Siegel, R.W. (1994). Nanophase Materials-Synthesis-Properties-Applications. Kluwer Academic Publishers, Drodrecht.

[67] Chikazumi, S. (1959). Physics of Magnetism. New York: John Wiley.

[68] Ammar, S., Jouini, N., Fiévet, F., Beji, Z., Smiri, L., Moliné,P., Danot, M., and Grenèche, J.M. (2006). Magnetic properties of zinc ferrite nanoparticles synthesized by hydrolysis in a polyol medium. *Journal of Physics: Condensed Matter, 18*(39): 9055-9069.

[69] George, M., John, A.M., Nair, S.S., Joy, P.A., and Anantharaman, M.R.(2006). Finite size effects on the structural and magnetic properties of sol–gel synthesized $NiFe_2O_4$ powders J. Magn. Magn.Mater. (302) 190–195.

[70] Sepelak, V., Menzel, M., Bergmann, I. Wiebcke, M., Krumeich, F., and Becker, K.D. (2004). Structural and magnetic properties of nanosize mechanosynthesized nickel ferrite. Journal of Magnetism and Magnetic Materials, 272-276(2): 1616-1618.

[71] Zhao, D., Wu, X., Guan, H., and Han, E. (2007). Study on supercritical hydrothermal synthesis of $CoFe_2O_4$ nanoparticles. Journal of Supercritical Fluids, 42(2): 226-233.

[72] Chaoquan, H., Zhenghong, G., and Xiaorui, Y. (2008). One-pot low temperature synthesis of MFe_2O_4 (M = Co, Ni, Zn) superparamagnetic nanocrystals. Journal of Magnetism and Magnetic Materials, 320(8): L70-L73.

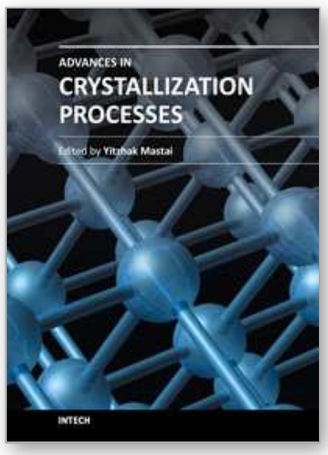

Advances in Crystallization Processes

Edited by Dr. Yitzhak Mastai

ISBN 978-953-51-0581-7
Hard cover, 648 pages
Publisher InTech
Published online 27, April, 2012
Published in print edition April, 2012

Crystallization is used at some stage in nearly all process industries as a method of production, purification or recovery of solid materials. In recent years, a number of new applications have also come to rely on crystallization processes such as the crystallization of nano and amorphous materials. The articles for this book have been contributed by the most respected researchers in this area and cover the frontier areas of research and developments in crystallization processes. Divided into five parts this book provides the latest research developments in many aspects of crystallization including: chiral crystallization, crystallization of nanomaterials and the crystallization of amorphous and glassy materials. This book is of interest to both fundamental research and also to practicing scientists and will prove invaluable to all chemical engineers and industrial chemists in the process industries as well as crystallization workers and students in industry and academia.

InTech Europe
University Campus STeP Ri
Slavka Krautzeka 83/A
51000 Rijeka, Croatia
Phone: +385 (51) 770 447
Fax: +385 (51) 686 166
www.intechopen.com

InTech China
Unit 405, Office Block, Hotel Equatorial Shanghai
No.65, Yan An Road (West), Shanghai, 200040, China
中国上海市延安西路65号上海国际贵都大饭店办公楼405单元
Phone: +86-21-62489820
Fax: +86-21-62489821

IntechOpen